

**DIRECTIONAL CORRELATION FROM ORIENTED STATES AND LINEAR
POLARIZATION MEASUREMENTS OF GAMMA RAYS FROM ^{190}Tl**

Tshifhiwa Elmon Madiba

Thesis presented in fulfillment of the requirements for the degree of Master of
Sciences at the University of the Western Cape.



Supervisor:

Dr. D.G. Roux

Dept. of Physics

University of the Western Cape

Co-supervisor:

Dr. R.A. Bark

iThemba LABS

January 2008

DECLARATION

I, Tshifhiwa Elmon Madiba, hereby declare that the work contained in this thesis is my own original work and that I have not previously in its entirety or in part submitted it at any university for a degree.

Signature:



UNIVERSITY *of the*
WESTERN CAPE

Date:

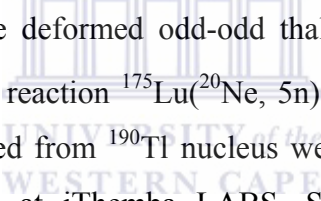
ABSTRACT

DIRECTIONAL CORRELATION FROM ORIENTED STATES AND LINEAR POLARIZATION MEASUREMENTS OF GAMMA RAYS FROM ^{190}Tl .

Tshifhiwa Elmon Madiba

January 2008

iThemba LABS, P.O. Box 722, Somerset West, 7129, South Africa



High-spin states in the oblate deformed odd-odd thallium nucleus ($^{190}_{81}\text{Tl}_{109}$) have been investigated through the reaction $^{175}\text{Lu}(^{20}\text{Ne}, 5n)^{190}\text{Tl}$ at a beam energy of 115 MeV. The gamma rays emitted from ^{190}Tl nucleus were detected with Ge detectors using the AFRODITE array at iThemba LABS, South Africa. Gamma-gamma coincidence data were obtained and used to construct the level scheme. In this work, **D**irectional **C**orrelations from **O**riented (DCO) state ratios and linear polarization anisotropies were measured in order to deduce spin and parity of energy levels in the decay scheme. It was possible to determine the spin and parity of two additional signature-partner bands which decay to the ground-state band.

ACKNOWLEDGEMENTS

I would like to express my sincere gratitude to the following people for making the realization of this thesis to be successfully:

- Dr D.G. Roux for his guidance through out the project, and being the best supervisor I could ever ask for.
- Dr R.A. Bark for supervision, support, encouragement and guidance throughout the duration of this project.. I am very grateful for allowing me pursue this project under your supervision.
- To Prof J.F Sharpey-Schaffer, I am grateful for his willingness to share knowledge with me and the reading of this thesis. Each discussions with you, has inspired me to work hard.
- To all AFRODITE staff at iThemba LABS and University of the Western Cape staff for their support and assistance they gave me throughout the duration of this project;
- To Prof R Lindsay, Dr J.J. Lawrie, Dr E.A Lawrie for accepting me in the Manus/Matsci Program.
- To C. Mukwevho and S. Matiwana for encouraging me to work hard and assistance during this work.
- I am very grateful to Mr. and Mrs. Madia for supporting and monitoring my studies in tertiary.
- To iThemba LABS and The National Research Foundation (NRF) for the financial support;

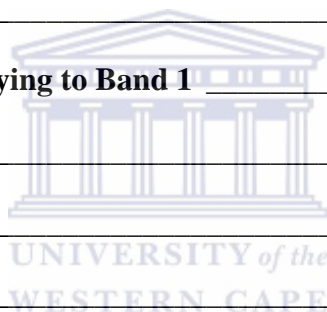
This work is dedicated to my grandmother (Miss K.L. Thamaha), my father (Mr.

M.W. Madiba) and Fulufhelo Madiba.

CONTENTS

CHAPTER 1	INTRODUCTION	1
1.1	Aim of the present work	1
CHAPTER 2	NUCLEAR THEORY	5
2.1	Nuclear deformation and its parameters	5
2.2	Nuclear rotation	9
2.3	Rotational bands	10
2.3.1	Rotational bands of even-even nucleus	10
2.3.2	Strongly-coupled bands	10
2.4	Heavy ion fusion reactions	11
2.5	Angular distribution of gamma rays	13
2.6	Angular correlations of gamma-rays	15
2.7	Directional correlations from oriented states	17
2.8	Interaction of Gamma Radiation with Matter	17
2.8.1	Photoelectric Effect	18
2.8.2	Pair Production	20
2.8.3	Compton Scattering	21
2.9	Linear polarization measurement of gamma rays	23
CHAPTER 3	EXPERIMENTAL TECHNIQUES	27
3.1	The AFRODITE array	27
3.1.1	Low energy photon spectrometer (LEPS) detectors	29
3.1.2	Clover detectors	29
3.2	Germanium detectors	32
3.3	Addback	33
3.4	Background Compton Suppression	33
3.5	The Experiment	34

CHAPTER 4	DATA ANALYSIS	35
4.1	Energy calibration and gain matching	35
4.2	Detector efficiency and efficiency calibration	37
4.3	Construction of gamma-gamma matrices	39
4.4	DCO Ratios	39
4.5	Linear polarization measurements	42
CHAPTER 5	RESULTS OF THE DATA ANALYSIS	44
5.1	DCO ratios	44
5.2	Linear polarization measurements	49
CHAPTER 6	SPIN AND PARITY ASSIGNMENT	52
6.1	Band 1	52
6.2	Energy levels decaying to Band 1	56
6.3	Band 2	58
6.4	Band 3	60
6.5	Band 4	62
6.6	Energy levels decaying to Band 4	64
6.7	Band 5	66
CHAPTER 7	SUMMARY AND CONCLUSION	67
	<i>Reference</i>	68



LIST OF FIGURES

1.1: The published level scheme of ^{190}Tl deduced following the $^{160}\text{Gd}(\beta^5\text{Cl}, 5n)^{190}\text{Tl}$ reaction at beam energies of 167 and 175 MeV. The energies are given in keV [Xie05, Zho05].	3
1.2: The level scheme of ^{190}Tl deduced using the AFRODITE array following the $^{175}\text{Lu}(^{20}\text{Ne}, 5n)^{190}\text{Tl}$ reaction at a beam energy of 115 MeV. The new energy levels have not yet been assigned spin and parity. The energies are given in keV [Bar07].	4
2.1: Different shapes of the nucleus corresponding to monopole, dipole, quadrupole and octupole deformation, shown with the dashed line on the figure.	6
2.2: Diagram showing the Lund convention. The β_2, γ plane is divided into three parts [And76].	8
2.3: Schematic view of the coupling of the collective angular momentum \vec{R} and the intrinsic angular momentum \vec{J} .	9
2.4: A schematic representation of a heavy ion fusion reaction illustrating the formation of a compound nucleus and the emission of different particles.	12
2.5: Schematic representation of how the angular momentum of an excited compound nucleus changes as it decays by first neutron and then by gamma-rays emission.	12
2.6: A gamma transition decay scheme.	13
2.7: Level scheme for two successive gamma rays.	15
2.8: Gamma correlation measurement set-up. Coincident measurements of consecutive gammas are performed [Kra73].	16
2.9: The process of photoelectric absorption.	19
2.10: The photoelectric effect mass coefficient dependence on the incident photon energy for lead [Kra88].	19
2.11: Pair production, conversion of γ energy into electron-positron pair [Lan03].	20
2.12: Schematic representation of the interaction of the incident photon and the loosely bound electron [Bus02].	22
2.13: Illustrates different regions where each of gamma-ray interaction dominates [Kno79].	22
2.14: Illustration of the principle of linear polarization measurements [Mor74].	23

3.1: The AFRODITE array with its supporting mechanical structure and the eighteen square facets of the target chamber. _____	28
3.2: The AFRODITE array and the arrangement of its clover and LEPS detectors. _____	28
3.3: The schematic view of the four segments of a clover detector [Jon95]. _____	30
3.4: A clover detector with tapered rectangular cryostat and cylindrical liquid nitrogen (LN2) dewar. _____	30
3.5: Polarization sensitivity (Q) of clover detectors as a function of the γ -ray energy [Sim83, Jon95]. _____	31
3.6: The schematic view of the BGO Compton suppression shield with a metal collimator at the front end. _____	33
4.1: The schematic mapping of the quadratic equation $E = a_0 + a_1x + a_2x^2$ and the linear equation $E = 0.5x'$. _____	36
4.2: The relative efficiency for the 90° and 135° clover detectors. _____	38
4.3: The total projection spectrum for the 135° clover detectors. _____	41
4.4: The total projection spectrum for the 90° clover detectors. _____	41
4.5: The total projection spectrum along the x -axis for the E_γ - E_γ ‘‘horizontal’’ matrix, showing γ -rays scattered parallel to the beam direction. _____	43
4.6: The total projection spectrum along the x -axis for the E_γ - E_γ ‘‘vertical’’ matrix, showing γ -rays scattered perpendicular to the beam direction. _____	43
5.1: The R_{DCO} values as a function of the mixing ratio [Mal06]. _____	44
5.2: The R_{DCO} values for the γ -transitions in the ^{190}Tl decay scheme obtained by setting gates on quadrupole transitions as a function of energy. _____	45
5.3: The γ - γ coincidence spectrum gated on the 552 keV transition detected in the 135° clover detectors. _____	46
5.4: The γ - γ coincidence spectrum gated on the 552 keV transition detected in the 90° clover detectors. _____	46
5.5: The R_{DCO} values for the γ -transitions in the ^{190}Tl decay scheme obtained by setting gates on stretched dipole transitions as a function on energy. _____	47
5.6: The γ - γ coincidence spectrum gated on 382 keV transitions detected in the 135° clover detectors. _____	48
5.7: The γ - γ coincidence spectrum gated on 382 keV transitions detected in the 90° clover detectors. _____	48

5.8: The polarization $P(\theta)$ values as a function of the mixing ratio. The dashed line indicates the plot for $\Delta I=0$ transitions. The solid line indicates the plot of $\Delta I=1$ [Bar07].	50
5.9: The linear polarization anisotropy as a function of energy.	51
6.1: The proposed level scheme of ^{190}Tl with spin and parity assigned. The energy levels are grouped into rotational bands. The energies are given in keV.	53
6.2: Coincidence spectrum obtained as a sum of spectra gated on the 552 keV, 709 keV, and 761 keV transitions.	54



LIST OF TABLES

2.1:	Indicates the sign of the linear polarization of γ -rays for different radiation type. ___	26
5.1:	Indicates the value of the linear polarization $P(\theta)$ of γ -rays for different radiation type. The γ -rays are of pure multipolarity. _____	49
6.1:	Gamma-ray energies, R_{DCO} ratios from coincidence spectra gated on quadrupole transitions, R_{DCO} ratios from coincidence spectra gated on dipole transitions, linear polarization anisotropy A_{P} , and spin and parity assignment for transitions in Band 1 of ^{190}Tl level scheme. _____	55
6.2:	Gamma-ray energies, spin and parity assignment, R_{DCO} ratios from coincidence spectra gated on quadrupole transitions, R_{DCO} ratios from coincidence spectra gated on dipole transitions, linear polarization anisotropy A_{P} for transitions in “Group A” of ^{190}Tl level scheme. _____	57
6.3:	Gamma-ray energies, R_{DCO} ratios from coincidence spectra gated on quadrupole transitions, R_{DCO} ratios from coincidence spectra gated on dipole transitions, linear polarization anisotropy A_{P} , and spin and parity assignment for transitions in Band 2 of ^{190}Tl level scheme. _____	59
6.4:	Gamma-ray energies, R_{DCO} ratios from coincidence spectra gated on quadrupole transitions, R_{DCO} ratios from coincidence spectra gated on dipole transitions, linear polarization anisotropy A_{P} , and spin and parity assignment for transitions in Band 3 of ^{190}Tl level scheme. _____	61
6.5:	Gamma-ray energies, R_{DCO} ratios from coincidence spectra gated on quadrupole transitions, R_{DCO} ratios from coincidence spectra gated on dipole transitions, linear polarization anisotropy A_{P} , and spin and parity assignment for transitions in Band 4 of ^{190}Tl level scheme. _____	63
6.6:	Gamma-ray energies, spin and parity assignment, R_{DCO} ratios from coincidence spectra gated on quadrupole transitions, R_{DCO} ratios from coincidence spectra gated on dipole transitions, linear polarization anisotropy A_{P} for transitions in “Group B” of ^{190}Tl level scheme. _____	65
6.7:	Gamma-ray energies, R_{DCO} ratios from coincidence spectra gated on quadrupole transitions, R_{DCO} ratios from coincidence spectra gated on dipole transitions, linear polarization anisotropy A_{P} , and spin and parity assignment for transitions in Band 5 of ^{190}Tl level scheme. _____	66

CHAPTER 1 INTRODUCTION

1.1 Aim of the present work

The initial purpose of the experiment was to search for chiral bands in the 190-mass region. The present work is a subset of the data analysis of this experiment: its goal is to assign spin and parity to the energy levels of the ^{190}Tl nucleus independent of any nuclear model. It is important to assign the correct spin and parity to new band structures in order to meaningfully discuss the intrinsic configurations, which is the basis of understanding the rotational behaviour of the nucleus.

Two techniques were employed to assign spin and parity. They are based on the directional correlation from oriented states (DCO) [Kra73, Krä89], and on the polarization of γ -rays. The DCO method is usually employed to determine the dipole and quadrupole nature of the γ -ray transitions. The second technique is used to assign the magnetic and electric nature of γ -ray transitions, making use of the high purity germanium clover detectors situated perpendicular to the beam direction [Sch94, Sch98].

During the data analysis of this experiment, results on ^{190}Tl were published by [Zho05] and [Xie05]. In those works, excited states in ^{190}Tl were populated by the $^{160}\text{Gd}(^{35}\text{Cl}, 5n)^{190}\text{Tl}$ reaction at beam energies of 167 MeV and 175 MeV. Figure 1.1 shows the level scheme obtained from the $^{160}\text{Gd}(^{35}\text{Cl}, 5n)^{190}\text{Tl}$ reaction. One rotational band with a negative parity was observed. The spins were tentatively assigned to the levels of another band, but with no parity suggested.

In the experiment performed at iThemba LABS, high spin states were populated using the $^{175}\text{Lu}(^{20}\text{Ne}, 5n)^{190}\text{Tl}$ reaction at beam energy of 115 MeV. A ^{175}Lu target of about 6 mg/cm^2 in thickness was used, which stopped the reaction products from escaping out of the target. The gamma rays emitted from the residual nuclei were detected with the high purity germanium detectors using the AFRican Omnipurpose for Innovative Techniques and Experiments (AFRODITE) array.

The current experiment allowed a much more extensive level scheme of ^{190}Tl to be constructed. The bands obtained by [Zho05, Xie05] were considerably extended to higher spins and three new rotational bands as well as several additional levels could be assigned to ^{190}Tl . This analysis was performed by Dr. R.A. Bark and the full level scheme of ^{190}Tl deduced from his analysis is shown in Figure 1.2. However no spin and parity were assigned. It was therefore important to measure the spin and parity of all new levels.

In this thesis we intend to describe various features of the nucleus and several techniques used to assign spin and parity of the energy levels as well as to show results obtained from the data analysis. The relevant nuclear theory and a few techniques used to assign spin and parity are discussed in Chapter 2. Chapter 3 describes the equipment available at iThemba LABS for studying the structure of the nucleus.

Chapters 4, 5, 6, and 7 form the main part of this thesis. In Chapter 4, the data analysis procedure is discussed in detail. Since theory on the DCO and polarization measurement is well understood, Chapter 5 compares the theoretical predictions and the experimental results. Chapter 6 outlines the arguments for spin and parity assignments in the ^{190}Tl decay scheme based on our results. Chapter 7 summarizes the main findings and indicates the direction of possible further research.

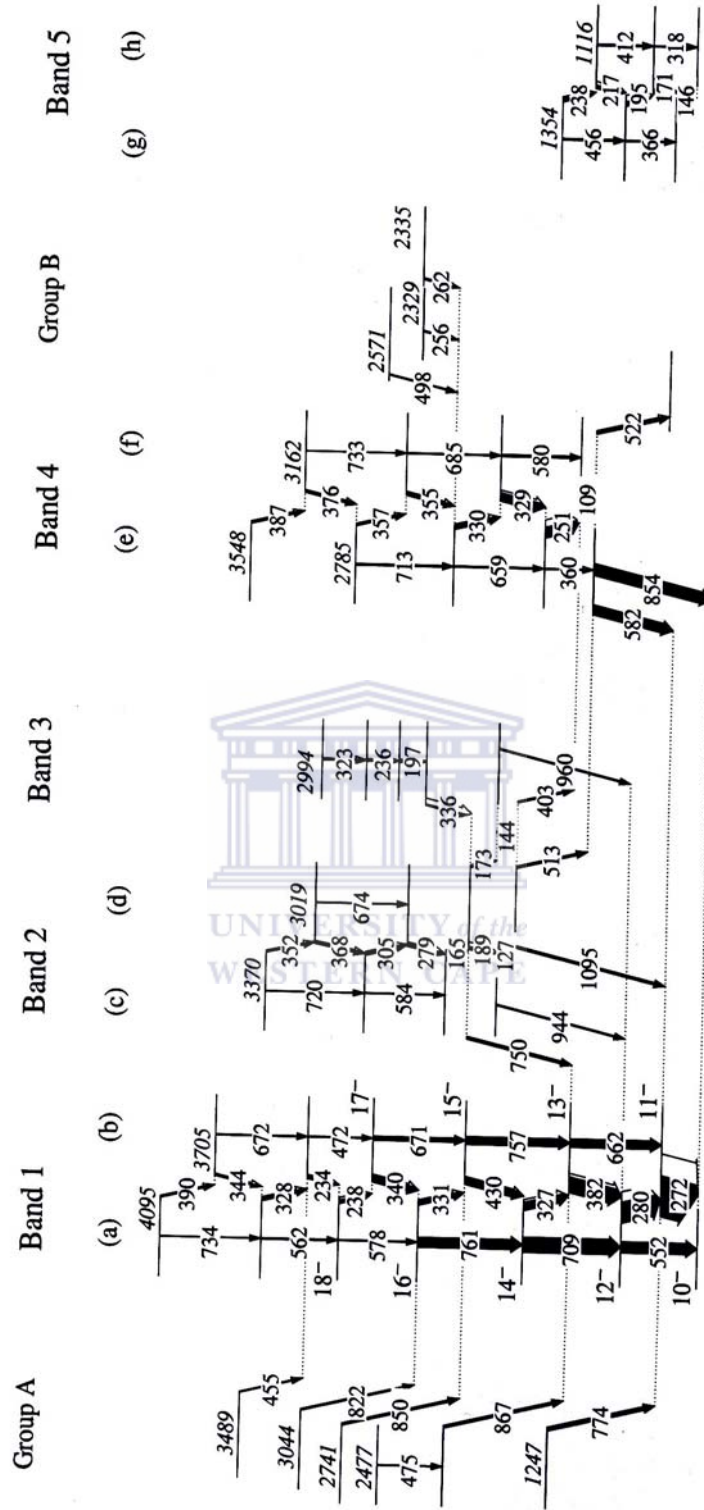


Figure 1.2: The level scheme of ^{190}Tl deduced using the AFRODITE array following the $^{175}\text{Lu}(^{20}\text{Ne}, 5n)^{190}\text{Tl}$ reaction at a beam energy of 115 MeV. The new energy levels have not yet been assigned spin and parity. The energies are given in keV [Bar07].

CHAPTER 2 NUCLEAR THEORY

The nucleus is treated as an isolated system and has a definite angular momentum often called nuclear spin and usually denoted with \vec{I} . The nuclear spin \vec{I} is composed of the angular momenta of all the individual nucleons, \vec{j}_i . In turn, the total angular momentum of a nucleon is defined as the sum of the orbital angular momentum, \vec{l}_i and spin \vec{s}_i : $\vec{j}_i = \vec{l}_i + \vec{s}_i$.

The total angular momentum of the nucleus can be generated by the vector addition of the individual nucleons angular momenta. This is known as single particle motion of the nucleus. The total angular momentum of the nucleus can also be generated by the motion of a whole nucleus, and this is referred as collective motion.

Another important quantum number used to characterize the nucleus is the parity usually denoted as π . The parity of a nucleus determines whether the nuclear wave function changes under the reflection through the origin of the coordinate system, and is given by $\pi = (-1)^L$, where L is the orbital angular momentum quantum number.

This chapter will discuss the deformation and rotation of the nucleus. It will also cover basic theory on relevant techniques to determine the nuclear spin and parity.

2.1 Nuclear deformation and its parameters

It is well established that many nuclei with Z protons and N neutrons number between the magic numbers are well deformed. The deformation of the nucleus arises from the way in which valence nucleons in a nucleus arrange themselves in nuclear orbital. The nucleus shape is described by:

$$R(\theta, \varphi) = R_0 \left[1 + \sum_{\lambda\mu} \alpha_{\lambda\mu} Y_{\lambda}^{\mu}(\theta, \varphi) \right] \quad (2.1)$$

where $Y_{\lambda}^{\mu}(\theta, \varphi)$ are spherical harmonics, $R(\theta, \varphi)$ is the distance from the centre of the nucleus to the surface, and R_0 is the radius of a sphere of the same volume. The $\alpha_{\lambda\mu}$ coefficients are the amplitudes of the spherical harmonics, which may be constant for a fixed nuclear shape or time dependent to describe a time varying distribution such as vibration and deformation [Lil01].

The deformation of the nucleus is one mode of collective excitation of the nucleus. There are several modes of deformation each characterized by λ . For instance, $\lambda = 0$ corresponds to the deformation of a monopole nuclear shape, and the $\lambda = 1$ coefficients describe the deformation in a dipole nuclear shapes. The $\lambda = 2$ term describes quadrupole deformations while the $\lambda = 3$ term describes octupole deformations [Hod97, Rin90]. The nuclear shapes for $\lambda = 0, 1, 2, 3$ values are shown in the Figure 2.1.

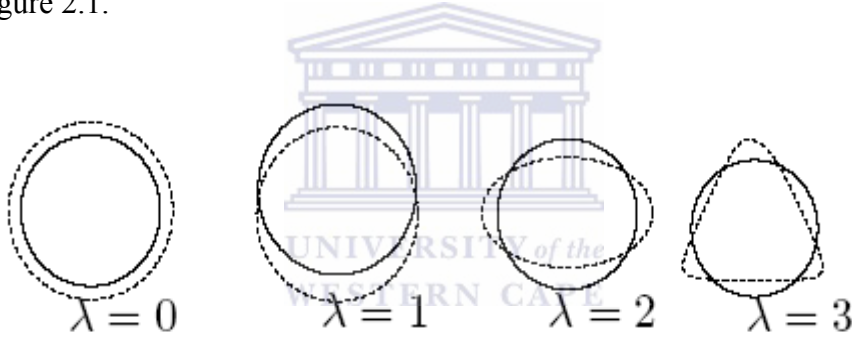


Figure 2.1: Different shapes of the nucleus corresponding to monopole, dipole, quadrupole and octupole deformation, shown with the dashed line on the figure.

For large deformations, it is better to describe the nuclear shape with respect to the body fixed axes rather than the laboratory axes, because if the body rotates, the $\alpha_{\lambda\mu}$ coefficients would change with time, even though we would say the nuclear shape remains the same [Bar07]. Considering only quadrupole distortions we get:

$$R(\theta', \varphi') = R_0 \left[1 + \sum_{\mu=-\lambda}^{\lambda} \alpha_{2\mu} Y_{2\lambda}(\theta', \varphi') \right] \quad (2.2)$$

where θ' , φ' and the $\alpha_{2\mu}$ coefficients refer to the body fixed system.

If the body fixed frame coincides with the principal axes, then the five possible quadrupole coefficients are reduced into two independent coefficients such that:

$$\alpha_{22} = \alpha_{2-2} \quad (2.3)$$

$$\alpha_{21} = \alpha_{2-1} = 0 \quad (2.4)$$

Another convention uses the Hill-Wheeler coordinates β_2 and γ , defined by [Hil53]:

$$\alpha_{20} = \beta_2 \cos \gamma \quad (2.5)$$

$$\alpha_{22} = \frac{1}{\sqrt{2}} \beta_2 \sin \gamma \quad (2.6)$$

The parameter γ measures the “triaxiality” of the nucleus. The parameter β_2 measures the total nuclear quadrupole deformation since it is related to the α_{20} and α_{22} coefficients through the equation:

$$\beta_2^2 = \sum_{\mu} |\alpha_{2\mu}|^2 = \alpha_{20}^2 + 2\alpha_{22}^2 \quad (2.7)$$

The parameters β_2 and γ are defined according to the Lund convention as shown in Figure 2.2. From Figure 2.2, the β_2, γ plane is divided into three parts. The sector between 0° and 60° contains all the nuclear shapes uniquely and may be taken as a representative one. The values of $\gamma = 0$ and $\gamma = -120^\circ$ correspond to prolate spheroids that rotate collectively and non-collectively around the principal axis, respectively. The values of $\gamma = 60^\circ$ and $\gamma = -60^\circ$ correspond to oblate deformation rotating non-collectively and collectively about the principal axis, respectively.

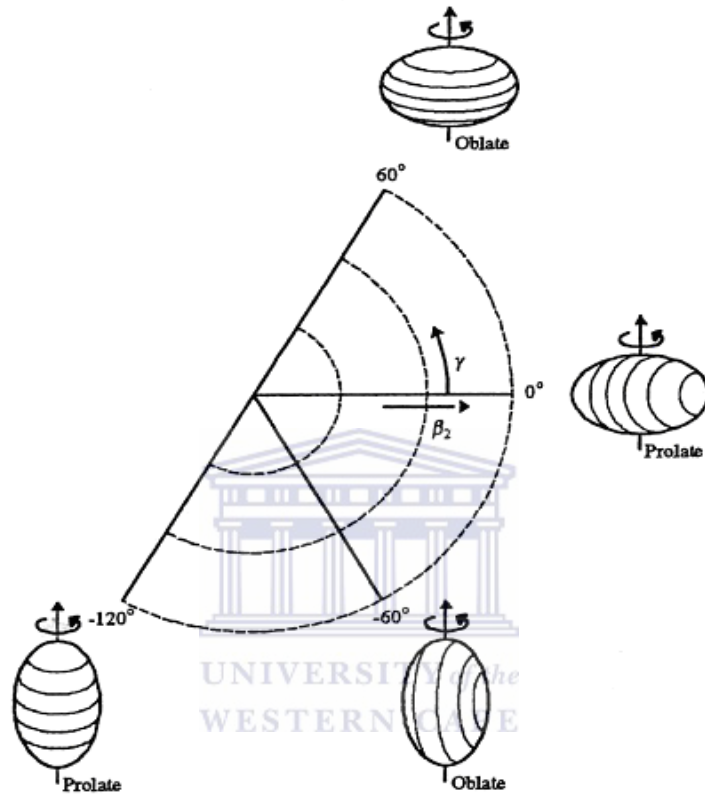


Figure 2.2: Diagram showing the Lund convention. The β_2, γ plane is divided into three parts [And76].

2.2 Nuclear rotation

The rotational motion of the nucleus is the likely mode of excitation of prolate or oblate deformed nuclei. The collective motion of nucleons will generate the rotational angular momentum \vec{R} . An additional angular momentum \vec{J} will be generated by the intrinsic motion of any unpaired nucleons outside of the core. The rotational angular momentum \vec{R} will be coupled with intrinsic angular momentum \vec{J} to give the total angular momentum \vec{I} of the nucleus with the form:

$$\vec{I} = \vec{R} + \vec{J} \quad (2.8)$$

where I is a constant of motion. The projection of the angular momentum onto the symmetry axis is $K\hbar$. The coupling of angular momentum is indicated in Figure 2.3.

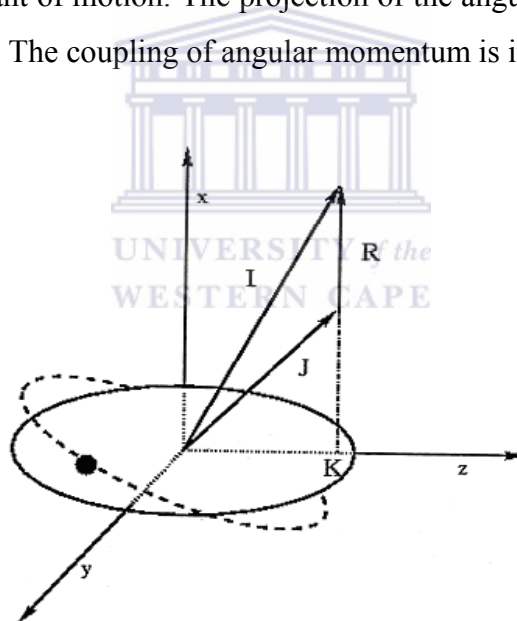


Figure 2.3: Schematic view of the coupling of the collective angular momentum \vec{R} and the intrinsic angular momentum \vec{J} .

2.3 Rotational bands

The rotation of a well-deformed nucleus will give rise to regular sequences of states with consecutively increasing angular momenta known as rotational bands. Generally, the excitation energy of the states in rotational bands is given by:

$$E_{exc}(I) = \frac{\hbar^2}{2J_0} I(I+1) \quad (2.9)$$

where J_0 is the moment of inertia which depends on the shape and the internal structure of the nucleus.

2.3.1 Rotational bands of even-even nucleus

The ground state band of deformed even-even nucleus consists of stretched E2 transitions built above the 0^+ ground state. All the nucleons are paired and the nucleus rotates as a whole around the rotational axis, which is perpendicular to the principal axis of the nucleus. The spins of the levels are given as:

$$I = 0, 2, 4, 6, \dots, \text{ For } K^\pi = 0^+ \quad (2.10)$$

where K is the projection of the angular momentum on the principal axis.

2.3.2 Strongly-coupled bands

These bands are observed for relatively large nuclear deformation and not very high rotational frequencies. The bands contain stretched M1 and E2 transitions. The spins and excitation energy allowed for these bands are then

$$I = K, K+1, K+2, \dots, \text{ For } K^\pi \neq 0 \quad (2.11)$$

$$E_{exc} = \frac{\hbar^2}{2J_0} [I(I+1) - K^2], \text{ For } K \neq \frac{1}{2} \quad (2.12)$$

2.4 Heavy ion fusion reactions

Heavy ion fusion reactions are the most important method of populating high spin states. Stable beam-target combinations can be used to populate neutron deficient nuclei at high spin. The formation and de-excitation of a compound nucleus is shown in Figure 2.4 and Figure 2.5. Figure 2.4 shows how the compound nucleus is formed and the emission of different particles. Figure 2.5 shows several features on how the angular momentum of an excited compound nucleus changes as it decays by first neutron and then by γ -ray emission.

For a heavy ion nuclear reaction to occur the projectile nucleus must have enough energy to overcome the Coulomb barrier that exists between itself and the target nucleus. The compound system obtains its excitation energy from the kinetic energy of collision in the center-of-mass and the reaction Q value.

During compound nucleus formation, a large amount of the orbital angular momentum will be transferred to the compound nucleus. The compound system will initially be highly excited, and will then de-excite through the evaporation of neutrons, protons and heavy charged particles (mainly α particles). Neutron evaporation is dominant when the compound nucleus lies far from the proton drip line.

When the difference in energy between the excited nucleus and the yrast line is insufficient to evaporate any more neutrons or charged particles, the nucleus loses its remaining energy and angular momentum by the emission of γ -rays. The “yrast” line is that sequence of states with lowest possible energy for a given angular momentum and is approximately 8 MeV below the particle evaporation threshold.

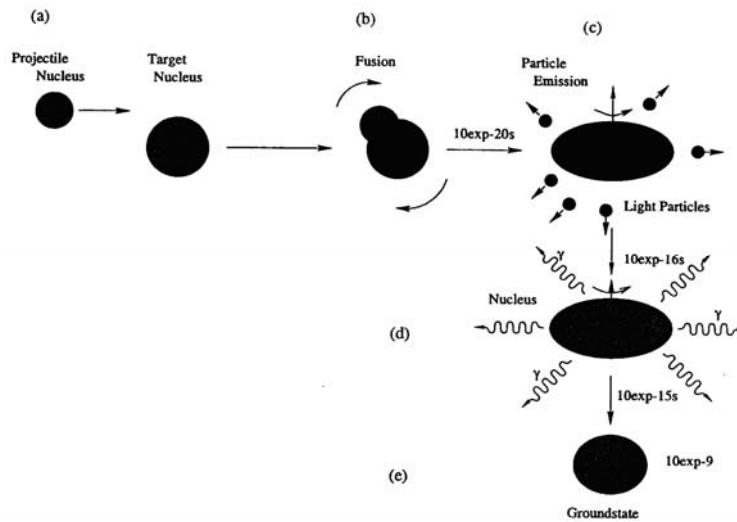


Figure 2.4: A schematic representation of a heavy ion fusion reaction illustrating the formation of a compound nucleus and the emission of different particles.

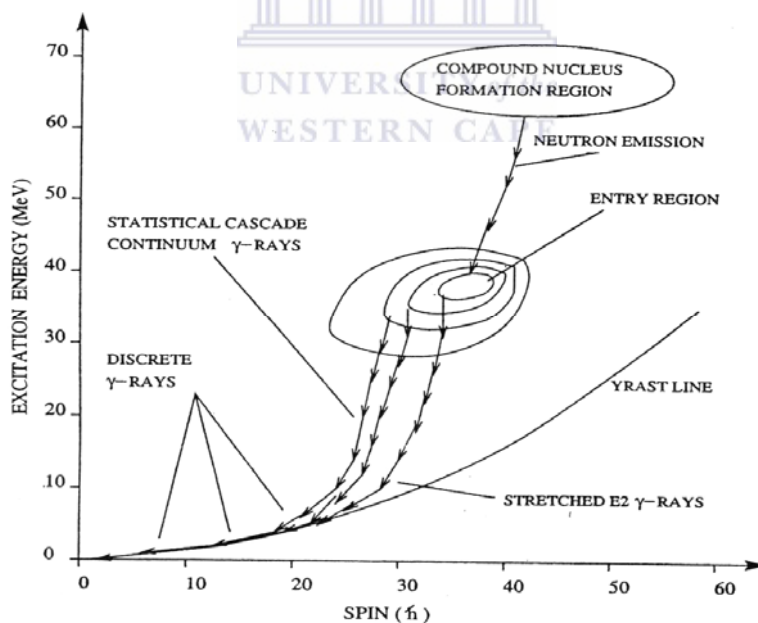


Figure 2.5: Schematic representation of how the angular momentum of an excited compound nucleus changes as it decays by first neutron and then by gamma-rays emission.

2.5 Angular distribution of gamma rays

Suppose a nucleus decays from initial state I_i to final state I_f as shown in Figure 2.6. As it decays from m_i -substate to m_f -substate, the angular distribution of the emitted radiation will have the form:

$$W(\theta) = \sum_i P(m_i) W_{m_i \rightarrow m_f}(\theta) \quad (2.13)$$

where $P(m_i)$ are the population parameters of the initial substate, i.e. the fraction of the nuclei that occupy the state m_i . If the m_i -substates are equally populated, then summing over all the magnetic substates will result in an isotropic angular distribution. Consequently, no information can be deduced about the multipole order of radiation.



Figure 2.6: A gamma transition decay scheme.

In order to produce an anisotropic distribution of the emitted radiation, the m_i -substates must be unequally populated. Thus, the nuclei must be oriented. Oriented nuclei can be prepared by bombarding a target nucleus with particles that are absorbed or scattered by the target nuclei. As previously mentioned, in heavy ion fusion reaction, the incoming particle brings in large amounts of angular momentum to the compound nucleus. The spin of the compound nucleus will be strongly aligned perpendicular to the beam direction, principally populating the $m=0$ substate. It is therefore assumed that the excited state I_i is strongly aligned with m -substate population parameters $P(m)$ centered at $m = 0$ [Ham75]. Therefore assuming a Gaussian distribution, the population parameters would have the form:

$$P(m) = \frac{e^{-\frac{m^2}{2\sigma^2}}}{\sum_{m'=-I}^I e^{-\frac{m'^2}{2\sigma^2}}} \quad (2.14)$$

Here, σ is the width of the substate distribution.

The angular distribution function in equation 2.13 can also be expressed in terms of the Legendre polynomials P_k :

$$W(\theta) = \sum_k a_k(I_i \lambda \lambda' I_f) P_k(\cos \theta) \quad (2.15)$$

where the angular distribution coefficients $a_k(I_i \lambda \lambda' I_f)$ are given by [Mor74]:

$$a_k(I_i \lambda \lambda' I_f) = \rho_k(I_i) \frac{1}{1+\delta^2} [F_k(I_f \lambda \lambda' I_i) + 2\delta F_k(I_f \lambda \lambda' I_i) + \delta^2 F_k(I_f \lambda' \lambda' I_i)] \quad (2.16)$$

where the statistical tensor $\rho_k(I_i)$ is given by [Yam67]:

$$\rho_k(I_i) = (2I_i + 1)^{1/2} \sum_{m_i} (-)^{I_i - m_i} \langle I_i m_i - m | k 0 \rangle P(m_i) \quad (2.17)$$

and

$$F_k(I_f \lambda \lambda' I_i) = (-)^{I_f - I_i - 1} [(2\lambda + 1)(2\lambda' + 1)(2I_i + 1)]^{1/2} \times \langle \lambda 1 \lambda' - 1 | k 0 \rangle W(I_i I_i \lambda \lambda'; k I_f) \quad (2.18)$$

The $\langle \lambda 1 \lambda' - 1 | k 0 \rangle$ are the Clebsch-Gordan coefficients, and $W(I_i I_i \lambda \lambda'; k I_f)$ are the Racah coefficients. The quantity δ is called the mixing ratio and is given by:

$$\delta = \frac{\langle I_f | \lambda' | I_i \rangle}{\langle I_f | \lambda | I_i \rangle} \quad (2.19)$$

The mixing ratio is a ratio of contribution of multipolarities in a mixed multipolarity gamma ray transition.

2.6 Angular correlations of gamma-rays

One method of creating oriented nuclei is by observing 2 consecutive gamma decays. For instance, consider two gamma rays emitted in cascade from initial nuclear state I_i to a final nuclear state I_f . If the nucleus decays by emitting γ_1 followed by γ_2 as indicated in Figure 2.7, the observation of γ_1 in a particular direction picks out a set of nuclei in the state I with an anisotropic distribution of spin directions and the distribution will persist until γ_2 is emitted and observed in coincidence with γ_1 .

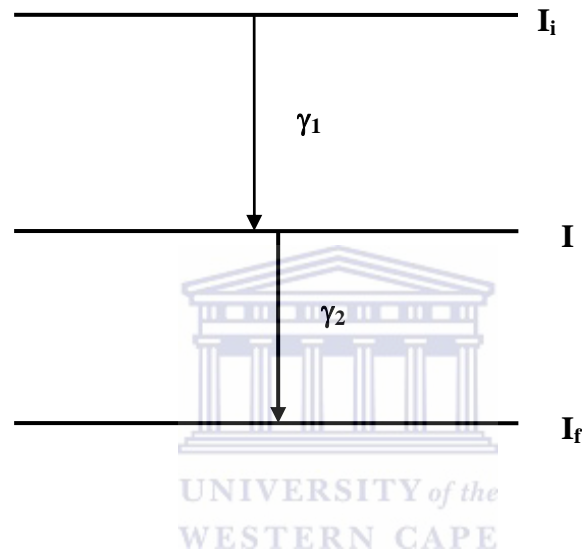


Figure 2.7: Level scheme for two successive gamma rays.

In angular correlations experiments, two detectors are placed at angles, θ_1 and θ_2 with respect to the beam direction and the angle between the detectors is ϕ as shown in Figure 2.8. The intensity of two γ -rays in coincidence at θ_1 and θ_2 i.e. the angular correlation function, is [Kra73]:

$$W(\theta_1, \theta_2, \phi) = N \sum_{\lambda_1 \lambda_2} Q B_{\lambda_1}(I_i) a_{\lambda_1}^{\lambda_2 \lambda_1}(\gamma_1) a_{\lambda_2}(\gamma_2) H_{\lambda_1 \lambda_2}(\theta_1, \theta_2, \phi) \quad (2.20)$$

Where N is a normalisation factor, and the indices λ , λ_1 and λ_2 are integers limited by the spins and multiplicities of the γ -ray transitions. $B_{\lambda_1}(I_i)$ are orientation parameters which depend on the substate population parameters:

$$B_{\lambda_1}(I_i) = (2I+1) \sum_m (-1)^{I+1} \langle I-m | I m | \lambda 0 \rangle P(m) \quad (2.21)$$

The $a_{\lambda}^{\lambda_2 \lambda_1}$ coefficients contain information on the nuclear wave function and spins of the states, multiplicities and mixing ratios of the transitions [Yam67].

$$a_{\lambda}^{\lambda_2 \lambda_1} = [F_{\lambda}^{\lambda_2 \lambda_1}(LLI_f I_i) + 2\delta F_{\lambda}^{\lambda_2 \lambda_1}(LL' I_f I_i) + \delta^2 F_{\lambda}^{\lambda_2 \lambda_1}(L' L' I_f I_i)] \frac{1}{1+\delta^2} \quad (2.22)$$

The F-coefficients are products of Wigner 3-j and 9-j symbols. The function $H_{\lambda_1 \lambda_2 \lambda}(\theta_1, \theta_2, \phi)$ describes the angular dependence. The main function of Q is to correct all geometric effects on the observed distribution function, including finite source as well as finite detector size. The Q value depends on the efficiency of a given detector, and also depends on the solid angle subtended by the detector. The angular correlation functions of the γ -rays depend on the spins of the involved levels, the multiplicities and the mixing ratio of the γ -transitions and the population of the distribution of the initial state.

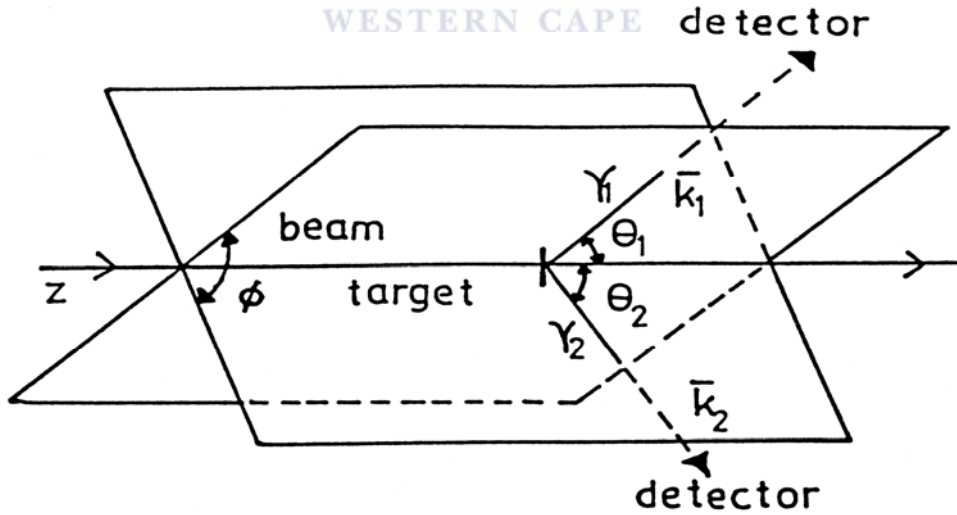


Figure 2.8: Gamma correlation measurement set-up. Coincident measurements of consecutive gammas are performed [Kra73].

2.7 Directional correlations from oriented states

The ratio of two angular correlation functions $W(\theta_1, \theta_2, \phi)$ and $W(\theta_2, \theta_1, \phi)$ can be used in determining the quadrupole and dipole nature of the γ -transitions in any nucleus of interest [Krä89]. This approach is known as Directional Correlations from Oriented states (DCO). The quadrupole or dipole nature of strong transitions can be investigated by placing detectors at a few different angles, while in the studies of weak transitions, large arrays of detectors are used. The directional correlation from an oriented state is given by:

$$R_{DCO} = \frac{W(\theta_1, \theta_2, \phi)}{W(\theta_2, \theta_1, \phi)} \quad (2.23)$$

Here, $W(\theta_1, \theta_2, \phi)$ is the intensity of γ_1 detected by detectors at θ_1 in coincidence with γ_2 detected by detectors at θ_2 , and $W(\theta_2, \theta_1, \phi)$ is the intensity of γ_1 detected by detectors at θ_2 in coincidence with γ_2 detected by detectors at θ_1 .

The corresponding experimental R_{DCO} ratio is given by:

$$R_{DCO} = \frac{I_{\theta_1}^{\gamma_2}(\text{Gate}_{\theta_2}^{\gamma_1})}{I_{\theta_2}^{\gamma_2}(\text{Gate}_{\theta_1}^{\gamma_1})} \quad (2.24)$$

where $I_{\theta_1}^{\gamma_2}(\text{Gate}_{\theta_2}^{\gamma_1})$ is the intensity of γ_2 determined from the spectrum in detectors at θ_1 gated on γ_1 detected by detectors at θ_2 , and $I_{\theta_2}^{\gamma_2}(\text{Gate}_{\theta_1}^{\gamma_1})$ is the intensity of γ_2 determined from the spectrum in detectors at θ_2 gated on γ_1 detected by detectors at θ_1 .

2.8 Interaction of Gamma Radiation with Matter

Gamma rays interact with matter through the following processes: photoelectric effect, pair production and Compton scattering. The three interaction processes are

briefly discussed below. The Compton scattering process is particularly important since we will make use of it in the determining γ -rays multipolarities.

2.8.1 Photoelectric Effect

Photoelectric effect is usually the most important interaction of low-energy gamma rays where all the photon energy is completely absorbed by the struck atomic electron as indicated in Figure 2.9. The struck electron, or photoelectron gains energy and escapes leaving the atom ionized. Thus the photon energy must exceed the binding energy of the photoelectron. The kinetic energy of the photoelectron is the incident photon energy (E_γ) less its binding energy (B_e).

$$T_e = E_\gamma - B_e \quad (2.25)$$

The gamma energy is given by $h\nu$, where ν is the frequency of the incident photon. The vacancy left in ionized atom by the ejected electron will be filled by the one of the electrons in the higher shell, and the ionized atoms de-excite to the ground state through the emission of x-rays. However, since the whole incident energy of the photon is deposited in the detector, the photoelectric effect can only be dominant at photon energies less than 200 keV for germanium. Figure 2.10 shows the photoelectric cross-section dependence on the incident photon energy. If the incident photon energy is greater than the binding energy of the electron, then less interaction between the photon and electron exists [Kra88]. The interaction depends upon atomic number Z with the absorption cross-section being approximated as:

$$\sigma \propto Z^n / E_\gamma^m \quad (2.26)$$

Here n is normally between 4 and 5 depending on the absorber material. The dependence explains the choice of high- Z material for shielding purposes and for use in γ detectors.

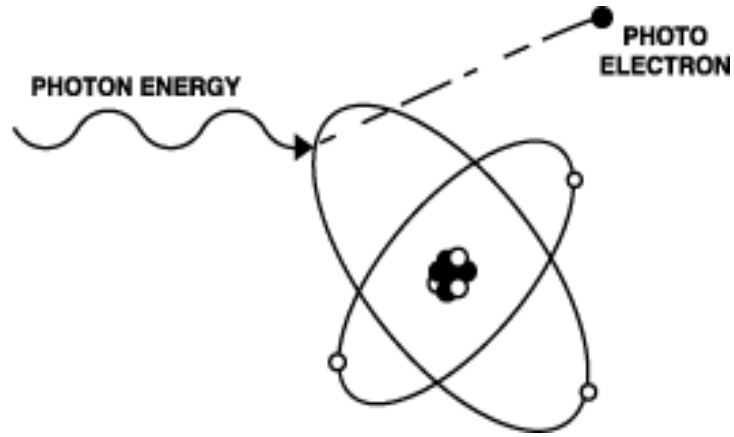


Figure 2.9: The process of photoelectric absorption.

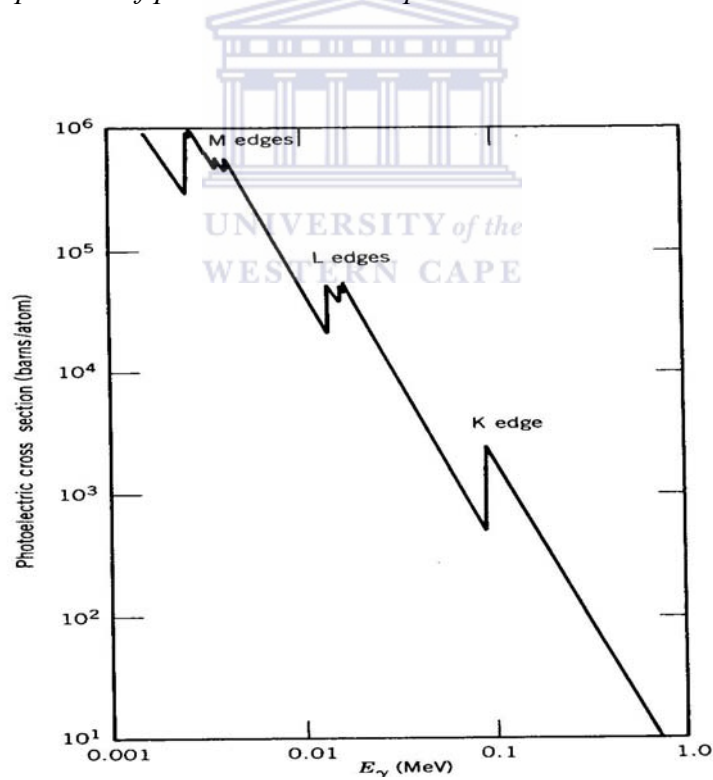


Figure 2.10: The photoelectric effect mass coefficient dependence on the incident photon energy for lead [Kra88].

2.8.2 Pair Production

In this process, the entire photon energy is converted by its interaction with the Coulomb field of a nucleus into the creation of an electron-positron pair as shown in Figure 2.11 [Lan03]. For pair production to take place, the gamma-ray energy must exceed the threshold energy of $2m_0c^2 \approx 1.022$ MeV. Any residual energy is distributed evenly between the electron and positron formed as kinetic energy of the form:

$$T_- + T_+ = E_\gamma - 2mc^2 \quad (2.27)$$

The positron is an anti-electron and after it slows down and comes to rest, it is attracted to an electron. Annihilation then takes place in which the electron and positron rest masses are converted into two γ -rays, each with energy of 511 keV. The annihilation γ -rays are emitted in the opposite direction in order to conserve momentum and they may interact in the absorbing medium by either photoelectric absorption or Compton scattering [Kno79].

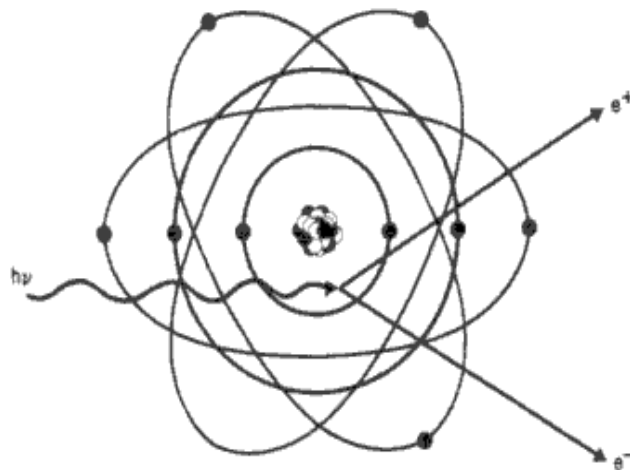


Figure 2.11: Pair production, conversion of γ energy into electron-positron pair [Lan03].

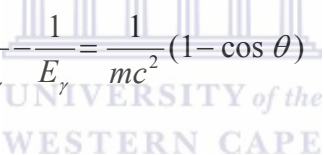
2.8.3 Compton Scattering

Compton scattering is an elastic scattering of a photon by a loosely bound atomic electron. In the process the incident photon is scattered at angle θ and as a result a fraction of its energy is transferred to the electron. The struck electron is scattered at an angle ϕ with a kinetic energy given by:

$$T = E_\gamma - E'_\gamma \quad (2.28)$$

where E_γ is the incident photon energy and E'_γ is the energy of the scattered photon. After this process the energy and frequency of the scattered photon is reduced. The struck atom is left ionized as it loses one of its electrons as shown in Figure 2.12.

From the conservation of energy and momentum, the following relation can be derived:


$$\frac{1}{E'_\gamma} - \frac{1}{E_\gamma} = \frac{1}{mc^2} (1 - \cos \theta) \quad (2.29)$$

The equation gives a minimum wavelength shift at 0° and maximum wavelength shift at 180° . Unlike in photoelectric effect, the incident photon is not absorbed by the loosely bound electron. Compton scattering is dominant in the 200-800 keV energy range. Most of the gamma rays emitted from rotational states in the nuclei fall within this range. The interaction probability decreases rapidly with increasing energy. The probability of Compton scattering per atom depends on the number of electrons available as scattering targets and therefore increases linearly with Z [Lil01].

Figure 2.13 indicates the energy regions where the processes of photoelectric effect, pair production, and Compton scattering are dominant.

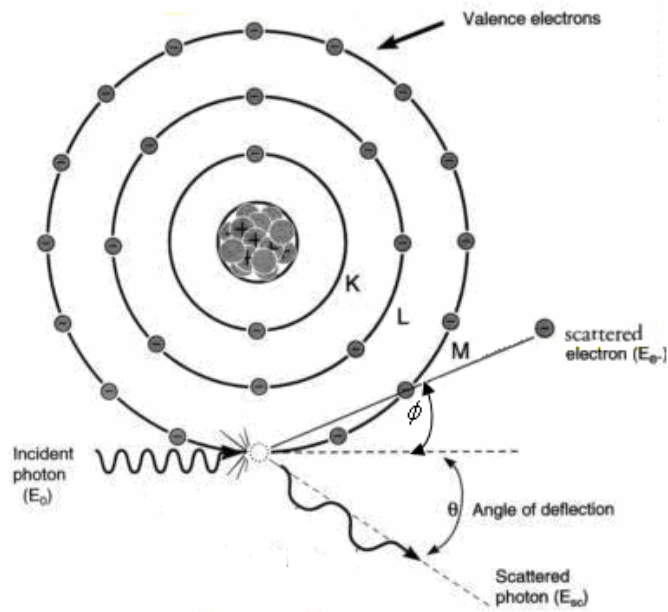


Figure 2.12: Schematic representation of the interaction of the incident photon and the loosely bound electron [Bus02].

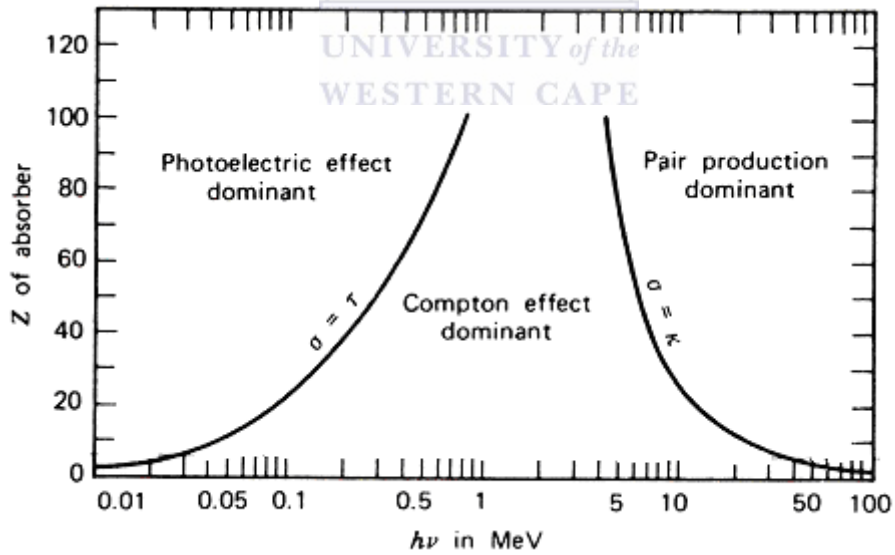


Figure 2.13: Illustrates different regions where each of gamma-ray interaction dominates [Kno79].

2.9 Linear polarization measurement of gamma rays

When a linearly polarized photon interacts with the electrons of a medium such as a detector, the photon causes the electron to oscillate along the electric field as indicated in Figure 2.14. The oscillating electron represents a linearly polarized electric dipole that preferentially emits a photon perpendicular to the polarization plane, permitting the linear polarization of the initial photon to be measured [Mor74]. The polarization plane is defined by direction of the electric vector \vec{E} . The linear polarization is defined as the difference between the intensities of the radiations presenting an electric vector parallel to the reaction plane defined by the beam axis and the outgoing of γ -rays, and those with electric vector perpendicular to that plane divided by their sum. Therefore the linear polarization takes the form:

$$P(\theta) = \frac{I(\theta, \phi = 0^\circ) - I(\theta, \phi = 90^\circ)}{I(\theta, \phi = 0^\circ) + I(\theta, \phi = 90^\circ)} \quad (2.30)$$

where $I(\theta, \phi = 0^\circ)$ is the intensity of the radiation presenting an electric vector parallel to the reaction plane, and $I(\theta, \phi = 90^\circ)$ is the intensity of the radiation presenting an electric vector perpendicular to the reaction plane.

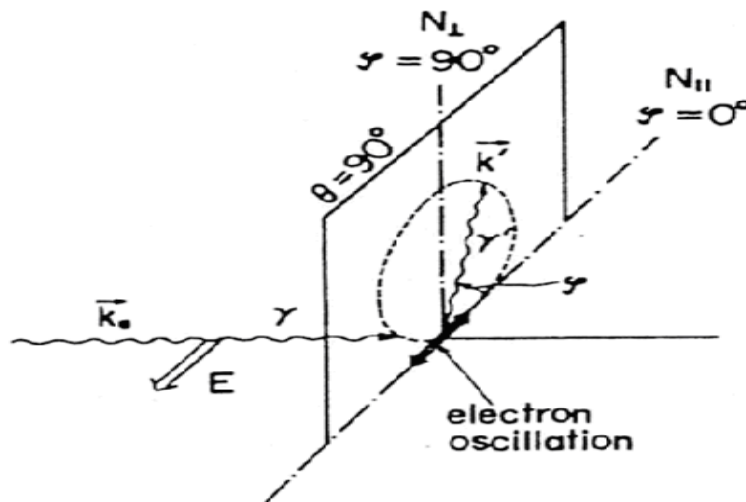


Figure 2.14: Illustration of the principle of linear polarization measurements [Mor74].

Experimentally, linear polarization measurements are performed with the aid of Compton linear polarimeters. The Compton linear polarimeter consists of at least two γ -ray detectors: a scatterer to scatter incident γ -rays and an analyzer to detect the γ -rays. The scatterer is fixed at an angle in the direction θ with respect to the beam direction while the analyzer is moved around the azimuthal angle ϕ . Since linear polarization measurements depend on the Compton scattering process, then the probability of an incident γ -radiation scattering through an angle ϕ depends upon the angle between the scattering plane containing θ and the plane normal to the electric vector E of the radiation as shown in Figure 2.14. The scattering plane is defined by the direction of the scattered γ -rays. The dependence of linear polarization on the Compton scattering can be obtained from the Klein Nishina cross-section formula:

$$\frac{d\sigma}{d\Omega} = \frac{r_0^2}{2} \left(\frac{E_\gamma'}{E_\gamma} \right)^2 \left(\frac{E_\gamma'}{E_\gamma} + \frac{E_\gamma}{E_\gamma'} - 2 \sin^2 \theta \cos^2 \phi \right) \quad (2.31)$$

Here, r_0 is the classical electron radius equal to $\frac{e^2}{mc^2}$, E_γ is the incident photon energy and E_γ' is the energy of the scattered photon. By measuring the number of γ -rays scattered perpendicular and parallel to the scattering plane, one performs the linear polarization anisotropy measurements. The linear polarization anisotropy A_p is defined as the difference between the number of γ -rays scattered perpendicular and parallel with respect to the beam direction divided by their sum:

$$A_p = \frac{aN_\perp - N_\parallel}{aN_\perp + N_\parallel} \quad (2.32)$$

where N_\perp and N_\parallel indicates coincidence counts perpendicular and parallel to the reaction plane, respectively. The coefficient a represents the relative efficiency of the detector. The linear polarization and the linear polarization anisotropy are related through the equation:

$$A_p = QP(\theta) \quad (2.33)$$

where Q is a measure of the sensitivity of a system of finite detectors to linear polarization. Using the theoretical definition of linear polarization as suggested by [Fag59] *et al.*, equation 2.30 can be expressed as:

$$P(\theta) = \pm \frac{\sum_k a_k^2 P_k^2(\cos \theta)}{\sum_k a_k P_k(\cos \theta)}, \quad k = 2, 4, \dots \quad (2.34)$$

Where a_k are the theoretical Legendre coefficients for the angular correlation of the γ -rays using a point detector not sensitive to polarization, and $P_k^2(\cos \theta)$ are the associate Legendre polynomials [Twi73]. In equation 2.34, the positive sign corresponds to electric radiations, and the negative sign to magnetic radiation. Considering pure dipole transitions, one can express the linear polarization function in equation 2.34 in terms of the angular distributions coefficient a_2 as:

$$P(\theta)^{M1} = \frac{3a_2 \sin^2 \theta}{2 - a_2 + 3a_2 \cos^2 \theta} \quad (2.35)$$

$$P(\theta)^{E1} = -\frac{3a_2 \sin^2 \theta}{2 - a_2 + 3a_2 \cos^2 \theta} \quad (2.36)$$

For pure quadrupole transitions, one gets the linear polarization in terms of the angular distributions coefficients a_2 and a_4 as [Lee02]:

$$P(\theta)^{M2} = -\frac{3a_2 \sin^2 \theta + a_4 \left(\frac{35}{4} \cos^4 \theta - 10 \cos^2 \theta + \frac{5}{4} \right)}{2 - a_2 + 3a_2 \cos^2 \theta + a_4 \left(\frac{35}{4} \cos^4 \theta - \frac{30}{4} \cos^2 \theta + \frac{3}{4} \right)} \quad (2.37)$$

$$P(\theta)^{E2} = \frac{3a_2 \sin^2 \theta + a_4 \left(\frac{35}{4} \cos^4 \theta - 10 \cos^2 \theta + \frac{5}{4} \right)}{2 - a_2 + 3a_2 \cos^2 \theta + a_4 \left(\frac{35}{4} \cos^4 \theta - \frac{30}{4} \cos^2 \theta + \frac{3}{4} \right)} \quad (2.38)$$

It is evident that equations 2.35, 2.36, 2.37 and 2.38 will give maximum linear polarization at $\theta = 90^\circ$. Since $\cos 90^\circ = 0$ and $\sin 90^\circ = 1$, then the above mentioned equations can be simplified as follows:

$$P(\theta)^{M1} = \frac{3a_2}{2 - a_2} \quad (2.39)$$

$$P(\theta)^{E1} = \frac{3a_2}{a_2 - 2} \quad (2.40)$$

$$P(\theta)^{M2} = -\frac{12a_2 + 5a_4}{8 - 4a_2 + 3a_4} \quad (2.41)$$

$$P(\theta)^{E2} = \frac{12a_2 + 5a_4}{8 - 4a_2 + 3a_4} \quad (2.42)$$

The coefficients a_2 and a_4 are given in literature and can be obtained from [Yam67]. The signs of linear polarization for different radiations are summarized in table 2.1.

Table 2.1: Indicates the sign of the linear polarization of γ -rays for different radiation type.

Radiation type	a_2	a_4	$P(\theta)$
Stretched M1	-	0	-
Unstretched M1	+	0	+
Stretched E1	-	0	+
Unstretched E1	+	0	-
Stretched M2	+	-	-
Stretched E2	+	-	+

CHAPTER 3 EXPERIMENTAL TECHNIQUES

The present chapter will discuss the equipment available at iThemba LABS for studying the structure of the nucleus. It will also describe the experiment analysed in this thesis.

3.1 The AFRODITE array

Gamma rays emitted from any heavy ion fusion reaction at iThemba LABS are detected by an array of detectors called AFRODITE. The abbreviation AFRODITE stands for AFRican Omni-purpose Detector for Innovative Techniques and Experiments. The AFRODITE array consists of two types of germanium detectors, namely clover detectors and low energy photon spectrometers detectors (LEPS) situated at 45° , 90° and 135° with respect to the beam direction. The AFRODITE array can accommodate a maximum of 8 clover detectors and 8 LEPS detectors.

The germanium detectors are placed in mechanical structure of rhombicuboctahedral shape as shown in Figure 3.1. The structure consists of eighteen square facets positioned at 0° , 45° , 90° , 135° , and 180° with respect to the beam direction. The target is mounted at the centre of the array, and the beam line passes through the 0° and 180° square facets.

All the germanium detectors are maintained at liquid nitrogen temperature in their own cryostats. The liquid nitrogen dewars are filled every 24 hours by an automatic filling system [Afr05]. The AFRODITE array is depicted in Figure 3.2.

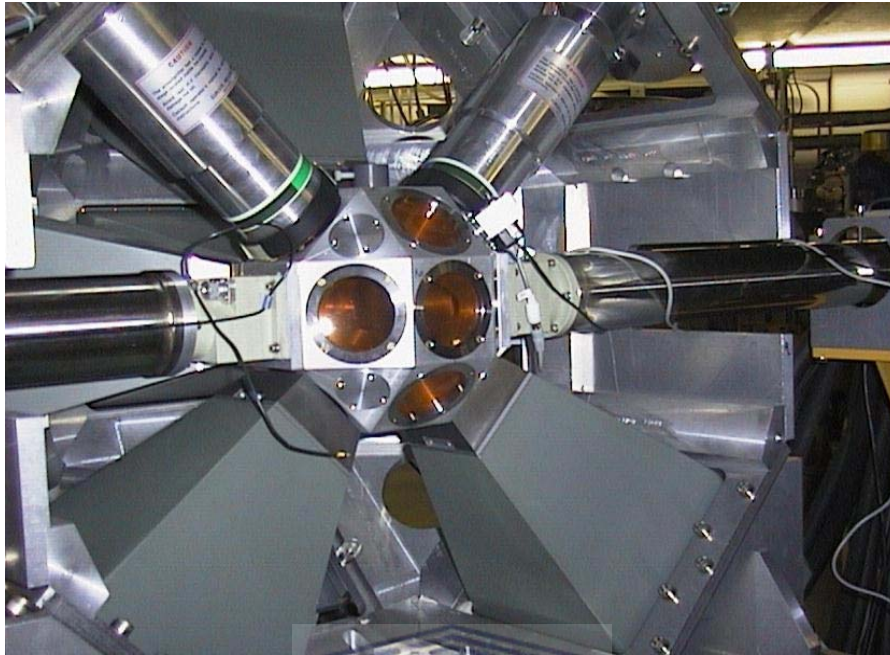


Figure 3.1: The AFRODITE array with its supporting mechanical structure and the eighteen square facets of the target chamber.

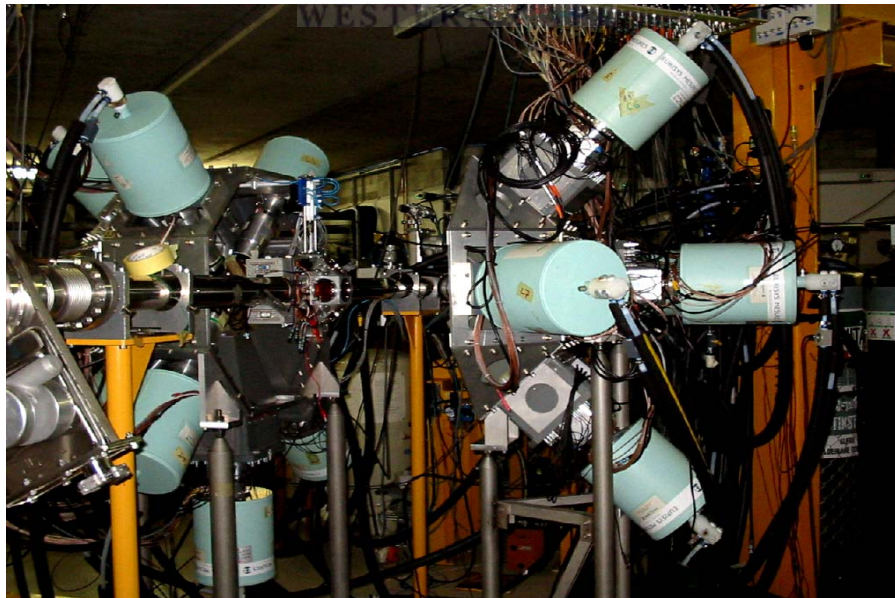


Figure 3.2: The AFRODITE array and the arrangement of its clover and LEPS detectors.

3.1.1 Low energy photon spectrometer (LEPS) detectors

The low energy photon spectrometer (LEPS) detectors are used in detecting γ -rays below 200 keV as well as x-rays. LEPS detectors consist of a single Ge crystal. Each planar crystal is electrically segmented into four quadrants. These crystals are intrinsic germanium of very high purity having a 60 mm diameter and 10 mm thickness.

3.1.2 Clover detectors

The clover detectors are used in observing high-energy γ -rays above 100 keV. They consist of four coaxial n-type Ge detectors, arranged like a four-leaf clover. Each detector has a square front face with round edges obtained by tapering it on two adjacent faces with an angle of 7.1° starting at around the half of the length and by cutting the two remaining faces parallel to the crystal axis and along its whole length. This enables a close packing of the detectors in the front with a Ge-Ge distance of about 0.2 mm and retains most (89%) of the original crystal volume. For Ge detectors of 50 mm diameter and 70 mm length as indicated in Figure 3.3, the remaining active volume in the clover detector is about 470 cubic centimeters. The detectors are held only by the rear-side which reduces the amount of material around the detector. The four detectors are mounted in a common cryostat of tapered rectangular shape as shown in Figure 3.4. To save space the gap between the tapered edges of the detectors and the inside of the cryostat is as small as 3.5 mm [Jon95].

Figure 3.5 shows the dependence of the polarization sensitivity Q of the clover detectors on the γ -rays energy. High polarization sensitivity is important for linear polarization measurements. The advantages of the clover detectors are:

- a reduction of the Doppler broadening due to the smaller opening angles of the individual crystals,
- a good energy resolution,
- a good timing response,
- a reduced vulnerability to neutron damage,
- a high sensitivity to the linear polarization of gamma-rays due to the presence of four crystals acting as polarimeter.

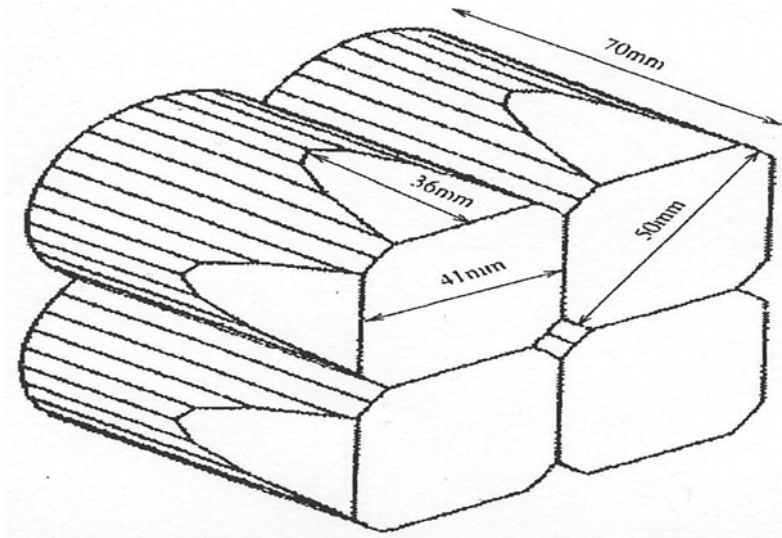


Figure 3.3: The schematic view of the four segments of a clover detector [Jon95].

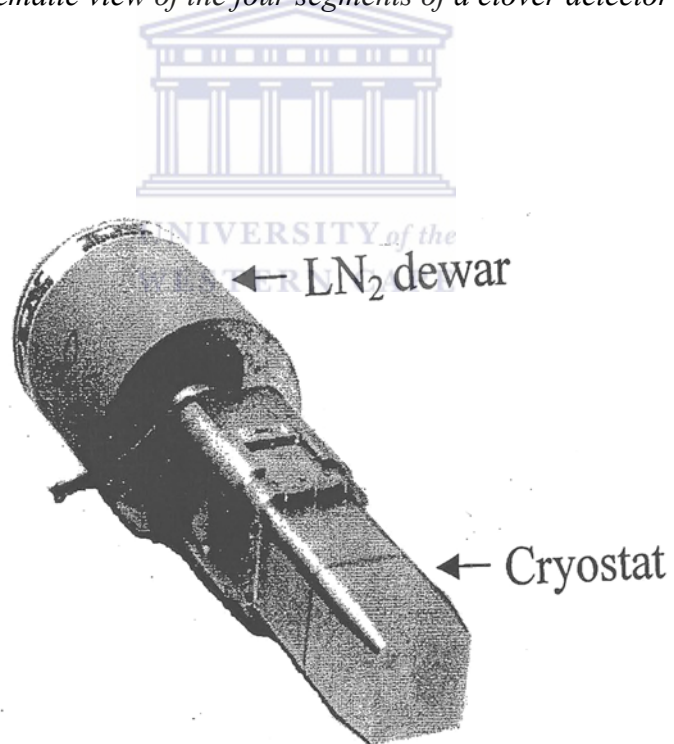


Figure 3.4: A clover detector with tapered rectangular cryostat and cylindrical liquid nitrogen (LN₂) dewar.

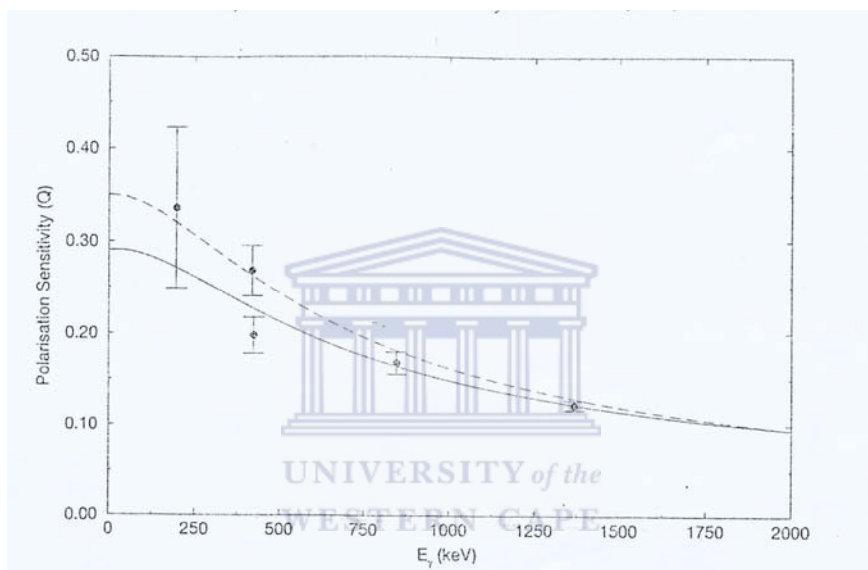


Figure 3.5: Polarization sensitivity (Q) of clover detectors as a function of the γ -ray energy [Sim83, Jon95].

3.2 Germanium detectors

Germanium detectors, similar to other semiconductor detectors, are large reverse-biased p-n junction diodes. At the junction between the p- and n-type material, the migration of electrons from the n-type material and holes from the p-type material gives rise to a region of net charge. This region is known as the depletion region. The net positive charge on one side of the junction, and the net negative charge on the other side, sets up an electric field gradient across the depletion region.

Any gamma ray interacting with the germanium material, through Compton scattering, photoelectric effect or pair production, will produce electron-hole pairs in the depletion region, which will then be swept to the edges of the detector because of the electric field, constituting an electric current.

Since the depletion region is the active part of the Ge detectors, it is required to be as large as possible. If a reverse bias is applied, the width of the depletion region can be increased. The width of depletion region is proportional to the bias voltage V applied through

$$d \approx \left(\frac{V}{N} \right)^{1/2} \quad (3.1)$$

Here, N is the impurity concentration of germanium. Therefore at a certain bias voltage, the width of the depletion region can only be increased if the impurity concentration N is reduced. High purity germanium (HPGe) has an impurity concentration of around one in 10^{12} atoms which allows a depletion region of several centimeters to be achieved. The minimum energy required for creating an electron-hole pair in germanium is approximately ~ 3 eV. A larger number of electron-hole pairs produced per MeV in germanium gives rise to better energy resolution.

3.3 Addback

If the gamma rays are Compton scattered from one segment to an adjacent segment of the clover detectors, the energy detected in both segments can be added to obtain the full energy of the γ -ray. This will enhance the photo-peak efficiency of the clover detectors especially for the γ -rays with high energy. This process is known as “addback”.

3.4 Background Compton Suppression

Gamma rays can either be fully absorbed by the HPGe detectors or Compton scattered out of the HPGe detector. In the last case, only part of the energy of the photon is absorbed, and this contributes to the background. This unwanted background is reduced by the use of the bismuth germanate (BGO) Compton suppression shield. The BGO shields are placed around each clover detector and run in anticoincidence with the clover detectors. The BGO shield has a heavy metal collimator placed in front of it so that γ -rays coming directly from the target position do not interact with the BGO material. Figure 3.6 show the BGO suppression shield with the collimator in front of it.

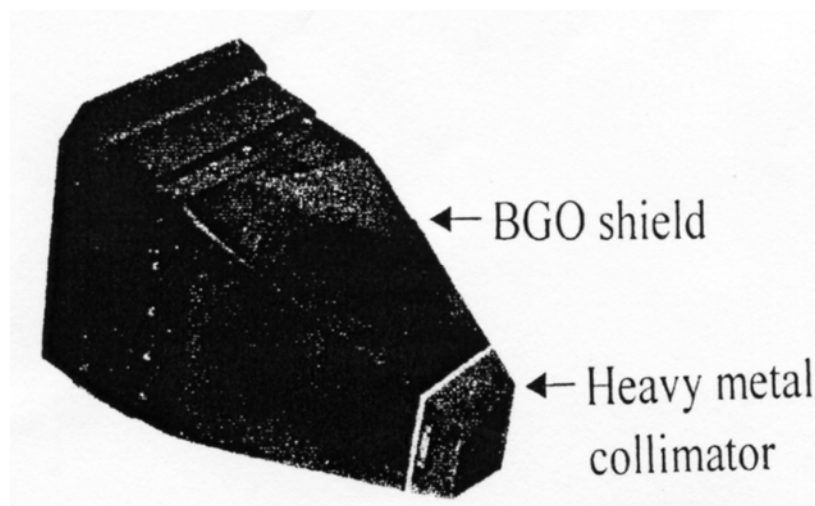


Figure 3.6: The schematic view of the BGO Compton suppression shield with a metal collimator at the front end.

3.5 The Experiment

High spin states in ^{190}Tl were populated through the $^{175}\text{Lu} (^{20}\text{Ne}, 5n)^{190}\text{Tl}$ reaction at a beam energy of 115 MeV. The ^{20}Ne beam was supplied by Separated-Sector Cyclotron (SSC), and a ^{175}Lu target with a natural abundance of 97 % was mounted inside the AFRODITE target chamber. The beam intensity on the target supplied by SSC was between 0.25 pA and 4 pA. The experiment was performed using both thin and thick ^{175}Lu targets. The experiment was run over three weekends.

In first weekend of the experiment, a thin (1 mg/cm^2) ^{175}Lu target was used as it was important to observe states at high spin. However, the detected γ -rays are emitted during a recoil of the residual nucleus, resulting in a Doppler shift for the γ -rays. The remaining two weekends were allocated for the use of thick (6 mg/cm^2) ^{175}Lu target as it was important to stop the $^{175}\text{Lu} (^{20}\text{Ne}, 5n)^{190}\text{Tl}$ reaction products from escaping out of the target. As a result, no Doppler shift occurred and best resolution was observed.

The gamma rays were detected using the AFRODITE array. The event rate of the AFRODITE array was 1.5 kHz for γ - γ coincidences. The trigger required that at least two clover detectors fired simultaneously in order to accept the event. The signals received during the experiments were transferred to the data room. The MIDAS software DAQ package was used to record data in event-by-event mode. The data were finally written on the Digital Linear Tapes (DLT). The details on the data acquisition system and the electronics set-up are discussed in [Mab03, Mal06, Ram06, Rou01].

The present analysis used the data obtained using the thick target in which approximately 3×10^8 γ - γ coincidence events were recorded with 8 clover detectors and 6 LEPS detectors. The set-up of the experiment was such that four clover detectors were placed at 90° , two clover detectors at 45° , and another two clover detectors at 135° .

CHAPTER 4 DATA ANALYSIS

It is necessary to calibrate the detectors with respect to both energy and efficiency because the detectors may perform differently from one experiment to the next. In order to proceed with the analysis, gamma-gamma matrices, DCO matrices, and linear polarization matrices were constructed.

4.1 Energy calibration and gain matching

The energy calibrations were performed before the start of the experiment using ^{152}Eu and ^{133}Ba sources. The spectra from these sources were recorded and centroids of known peaks were determined using SFIT program. The program SCAL was employed to determine the energy calibration coefficients through the quadratic equation $E = a_0 + a_1x + a_2x^2$.

The coefficients a_0 , a_1 , and a_2 differ for each element of the clover detectors. The quadratic equation $E = a_0 + a_1x + a_2x^2$ was mapped to the linear equation $E = 0.5x'$ as shown in Figure 4.1. Therefore equating the two equations, the following relation will hold:

$$x' = 2a_0 + 2a_1x + 2a_2x^2 \quad (4.1)$$

This implies that every gain matching coefficient must be multiplied by a factor of two. The gain drifts in the γ -rays peaks were also checked and corrected.

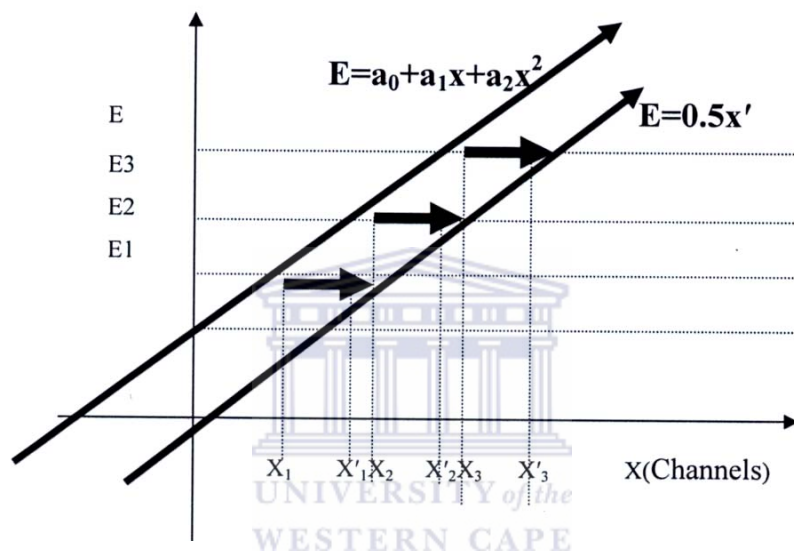


Figure 4.1: The schematic mapping of the quadratic equation $E = a_0 + a_1x + a_2x^2$ and the linear equation $E = 0.5x'$.

4.2 Detector efficiency and efficiency calibration

The detector efficiency is a measure of how many pulses occur for a given gamma or x-rays. There are various types of efficiency definitions for gamma rays detectors, such as absolute efficiency, intrinsic efficiency and relative efficiency. The absolute efficiency of gamma ray detector is the number of counts produced by a detector to the number of gamma rays emitted by the source. Intrinsic efficiency is defined as the ratio of counts produced by a detector to the number of gamma rays striking the detector.

Relative efficiency (ϵ) is the efficiency of one detector relative to another detector. The relative efficiency of a detector is influenced by the type of detecting material, size and shape of the detector, the energies of the radiation, the distance between the source, and the medium between the source and the detector [Leo87].

The efficiency calibration measurements of the clover and LEPS detectors were performed at the end of the experiment using ^{152}Eu and ^{133}Ba sources. The sources were mounted alternatively inside the target chamber. The relative efficiency (ϵ) of each detector was fitted using the Radware program *effit* [Rad95] as follows.

$$\ln(\epsilon) = [(A + Bx + Cx^2)^{-G} + (D + Ey + Fy^2)^{-G}]^{-1/G} \quad (4.2)$$

The constants A, B, C, D, E, F and G represent fitting parameters generated by the *effit* program. The parameter G determines the shape of the turn-over region between the high and low energy efficiency curve.

The relative efficiency (ϵ) curves for the 8 clover detectors situated at 135° and 90° in the AFRODITE array are shown in Figure 4.2. The Figure shows that clover detectors in the AFRODITE had maximum relative efficiency in the energy range 130-140 keV. The efficiency of the 135° clover detectors is 30 % bigger than the 90° clover detectors, and this is due to the fact one clover detectors in the 90° detectors was missing during the efficiency calibration.

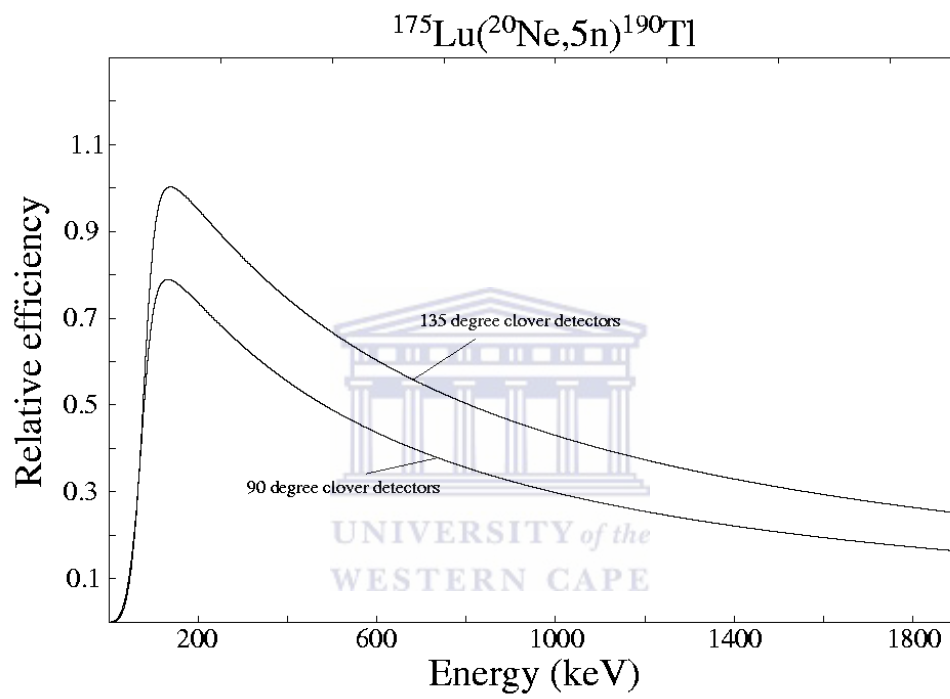


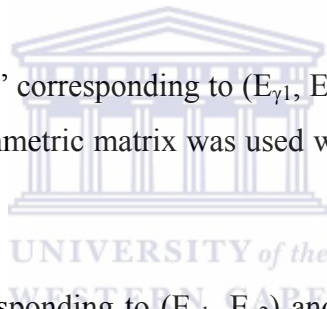
Figure 4.2: The relative efficiency for the 90° and 135° clover detectors.

4.3 Construction of gamma-gamma matrices

The normal approach to the analysis of γ - γ coincidences is for each event to store the energies of the two detected γ -rays into a two dimensional histogram, usually referred to as a matrix. Each axis of the matrix corresponds to the energy of the detected γ -rays.

For instance, let us assume two coincident γ -rays, $(E_{\gamma_1}, E_{\gamma_2})$ are emitted from a nucleus. The matrix is constructed by incrementing a two dimensional histogram at the coordinates $(E_{\gamma_1}, E_{\gamma_2})$ and $(E_{\gamma_2}, E_{\gamma_1})$ where the first member of the ordered pair denotes the x-coordinates and the second member of the ordered pair denotes the y-axis. The matrices are 4096×4096 channels corresponding to the energy range of about 2 MeV.

Since the counts in the “pixel” corresponding to $(E_{\gamma_1}, E_{\gamma_2})$ and $(E_{\gamma_2}, E_{\gamma_1})$ are equal, the matrix is symmetric. The symmetric matrix was used with ESCL8r in construction of the level scheme.



If counts in the “pixel” corresponding to $(E_{\gamma_1}, E_{\gamma_2})$ and $(E_{\gamma_2}, E_{\gamma_1})$ are not equivalent, then the matrix is asymmetric. Two different types of asymmetric matrix were constructed in the analysis of DCO and linear polarization measurements as discussed in section 4.4 and 4.5.

4.4 DCO Ratios

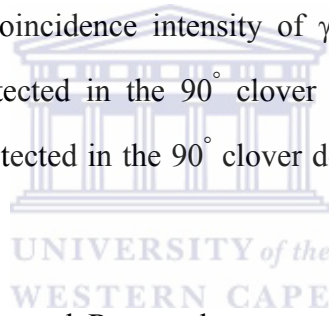
In order to deduce information about the multiplicities of γ -ray transitions observed in the ^{190}Tl level scheme, two DCO coincidence asymmetric matrices were constructed. The first matrix contained γ -rays detected at the 135° clover detectors (y-axis) in coincidence with the γ -rays detected at the 90° clover detectors (x-axis). The second matrix was the transpose of the first matrix.

The total projection of the matrix is obtained by projection of all counts onto one energy axis, which results in a one-dimensional γ -ray spectrum. Figure 4.3 and Figure

4.4 show the total projection spectrum for the DCO matrices. The Figures indicate that the γ -ray intensities of stretched dipole transitions detected at the 135° clover detectors are less than the γ -ray intensities of the same transitions detected at the 90° clover detectors. An example of such stretched dipole transition is the 387 keV transition. However, the γ -ray intensities of stretched quadrupole transitions detected at the 135° clover detectors is greater than the γ -ray intensities of the same transitions detected at the 90° clover detectors. An example of such a stretched quadrupole transition is the 624 keV transition. The R_{DCO} ratio of any γ -transition using the AFRODITE spectrometer array is defined by:

$$R_{DCO} = \frac{I(135^\circ, 90^\circ)}{I(90^\circ, 135^\circ)} \quad (4.3)$$

where $I(135^\circ, 90^\circ)$ is the coincidence intensity of γ_1 detected in the 135° clover detectors and γ_2 that is detected in the 90° clover detectors. $I(90^\circ, 135^\circ)$ is the coincidence intensity of γ_1 detected in the 90° clover detectors and γ_2 that is detected in the 135° clover detectors.



The uncertainties in the measured R_{DCO} values were calculated using the formula below:

$$\Delta R_{DCO} = R_{DCO} \sqrt{\left(\frac{\Delta I(135^\circ, 90^\circ)}{I(135^\circ, 90^\circ)}\right)^2 + \left(\frac{\Delta I(90^\circ, 135^\circ)}{I(90^\circ, 135^\circ)}\right)^2} \quad (4.4)$$

where $\Delta I(135^\circ, 90^\circ)$ is the uncertainty in $I(135^\circ, 90^\circ)$ and $\Delta I(90^\circ, 135^\circ)$ is the uncertainty in $I(90^\circ, 135^\circ)$. The R_{DCO} values were efficiency corrected by taking in consideration the efficiency of the 135° clover detectors and 90° clover detectors. In order for the relative efficiency at both 135° and 90° clover detector to cancel out, it is assumed that the efficiency at 135° clover detectors is three quarters that of the 90° clover detectors i.e. $\varepsilon(135^\circ) = \frac{3}{4}\varepsilon(90^\circ)$.

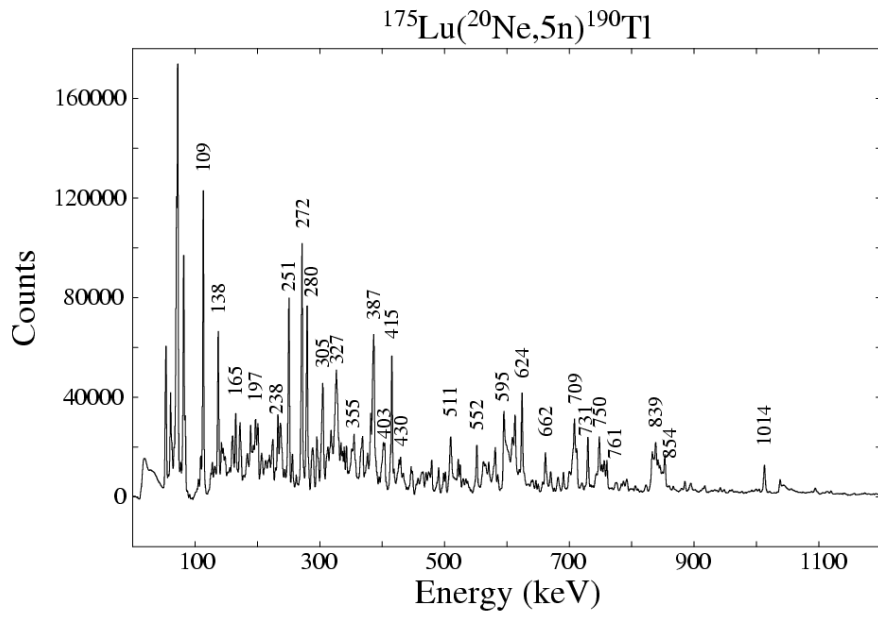


Figure 4.3: The total projection spectrum for the 135° clover detectors.

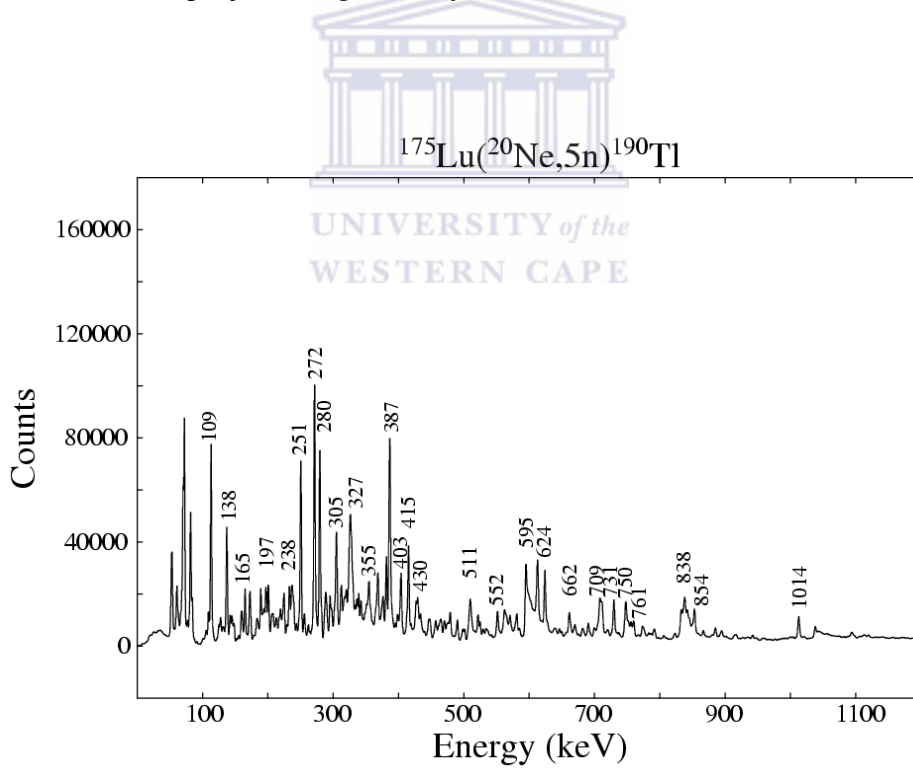


Figure 4.4: The total projection spectrum for the 90° clover detectors.

4.5 Linear polarization measurements

Clover detectors situated perpendicular to the beam direction were used to measure the linear polarization of the γ -rays observed in ^{190}Tl . Linear polarization anisotropies were deduced by constructing of two E_γ - E_γ matrices. The first matrix contained γ -rays, scattered perpendicular to the beam direction in the 90° clover detectors, in coincidence with any detected γ -ray. The second matrix contained γ -rays, scattered parallel to the beam direction in the 90° clover detectors, also in coincidence with any detected γ -ray. The total projection spectra for the polarization matrices are indicated in Figure 4.5 and Figure 4.6.

The linear polarization anisotropy A_P of any γ -transition using the AFRODITE spectrometer array is defined as:

$$A_P = \frac{N_V - N_H}{N_V + N_H} \quad (4.5)$$

N_V and N_H is the number of the γ -rays that scattered perpendicular and parallel with respect to the beam direction, respectively, as seen in a spectrum obtained by setting a gate on all the clover detectors. The uncertainty in the linear polarization anisotropy was calculated as follows:

$$\Delta A_P = \frac{2}{(N_V + N_H)^2} \sqrt{(N_H \sigma_v)^2 + (N_V \sigma_H)^2} \quad (4.6)$$

σ_v is the uncertainty of the number of γ -rays that scattered vertically seen by the 90° clover detectors crystals. σ_H is the uncertainty of the number of γ -rays that scattered horizontally seen by the 90° clover detectors crystals.

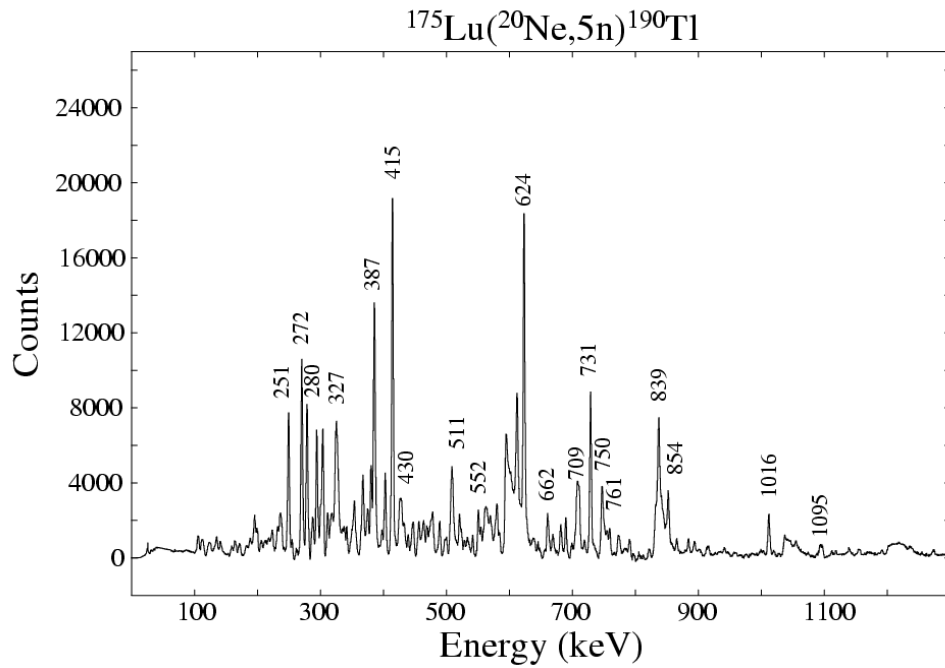


Figure 4.5: The total projection spectrum along the x-axis for the E_γ - E_γ 'horizontal' matrix, showing γ -rays scattered parallel to the beam direction.

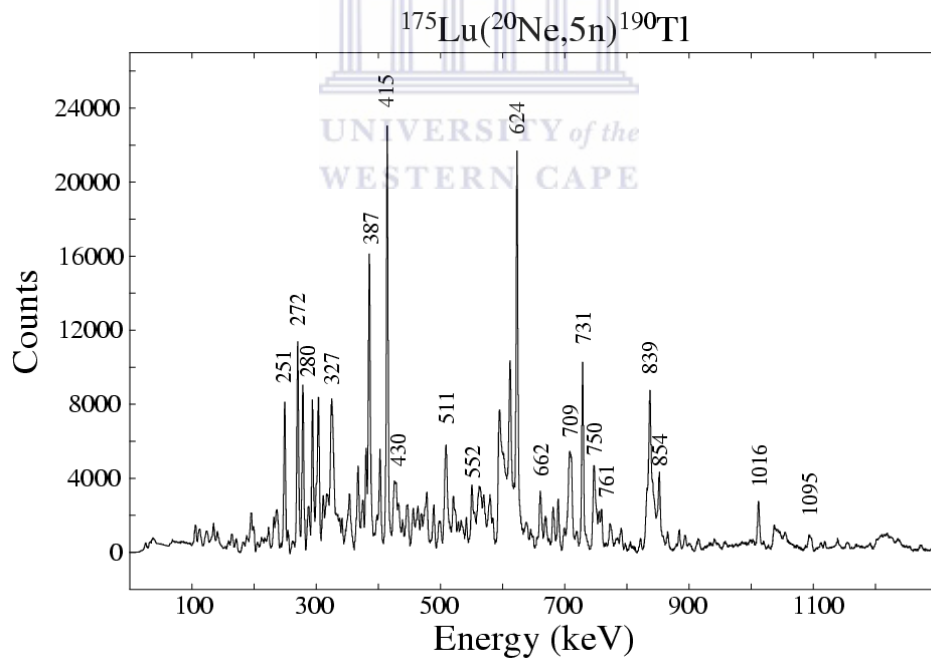


Figure 4.6: The total projection spectrum along the x-axis for the E_γ - E_γ 'vertical' matrix, showing γ -rays scattered perpendicular to the beam direction.

CHAPTER 5 RESULTS OF THE DATA ANALYSIS

5.1 DCO ratios

The R_{DCO} values expected for a stretched dipole and stretched quadrupole transitions depend strongly on the configuration of the spectrometer array, as well as the multipolarity of the gating transition. Recent R_{DCO} calculations by [Mal06] for the AFRODITE array suggested that $\Delta I=2$ cross-over transitions will have R_{DCO} values of ~ 1 while pure $\Delta I=1$ direct transitions will have R_{DCO} values of ~ 0.61 when the gating transition is a stretched quadrupole and when $\sigma/I \approx 0.33$. Therefore R_{DCO} of transitions in a common band of ^{190}Tl decay scheme must be compared with the R_{DCO} calculations by [Mal06] using the program DCO PLOT. Figure 5.1 shows that the R_{DCO} strongly depend on the mixing ratio. It is evident from the figure that single R_{DCO} value can correspond to more than one mixing ratio value.

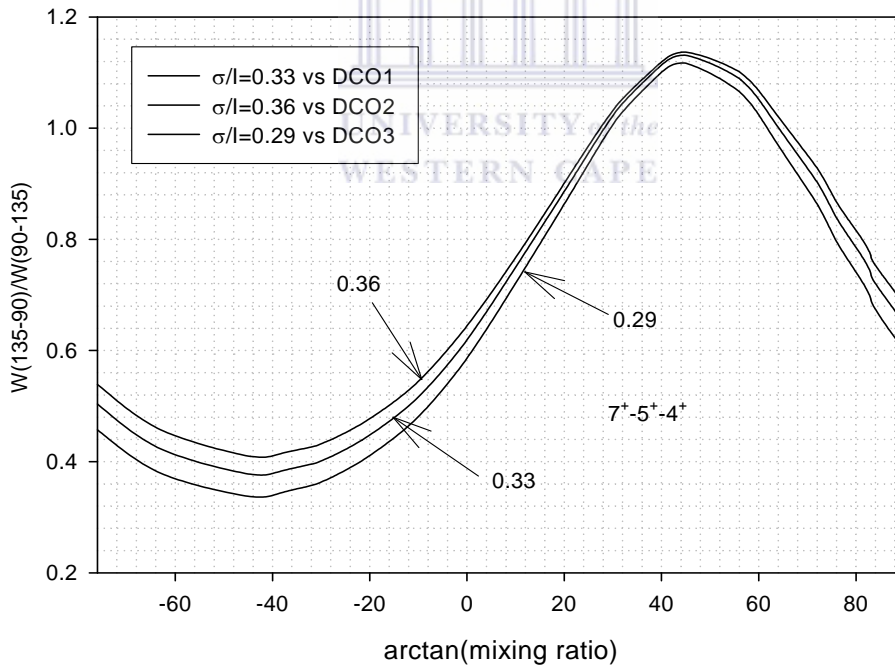


Figure 5.1: The R_{DCO} values as a function of the mixing ratio [Mal06].

The R_{DCO} values were obtained by first setting gates on known stretched quadrupole transitions. It is better to use background-subtracted spectra when measuring accurately R_{DCO} values. Figure 5.2 shows the R_{DCO} values as a function of γ -ray energy for different transitions in band from coincidence spectrum gated on quadrupole transitions. The Figure shows that the $\Delta I=2$ cross-over transitions in a band tend to cluster around R_{DCO} values of 1, and $\Delta I=1$ direct transitions in a band tend to cluster around R_{DCO} values of 0.6. The average R_{DCO} value of $\Delta I=2$ cross-over transitions in ^{190}Tl decay scheme was 0.99(7) while the average R_{DCO} value for $\Delta I=1$ direct transitions in ^{190}Tl decay scheme was 0.58(5). Therefore the typical R_{DCO} values are consistent with the theoretical values suggested by [Mal06].

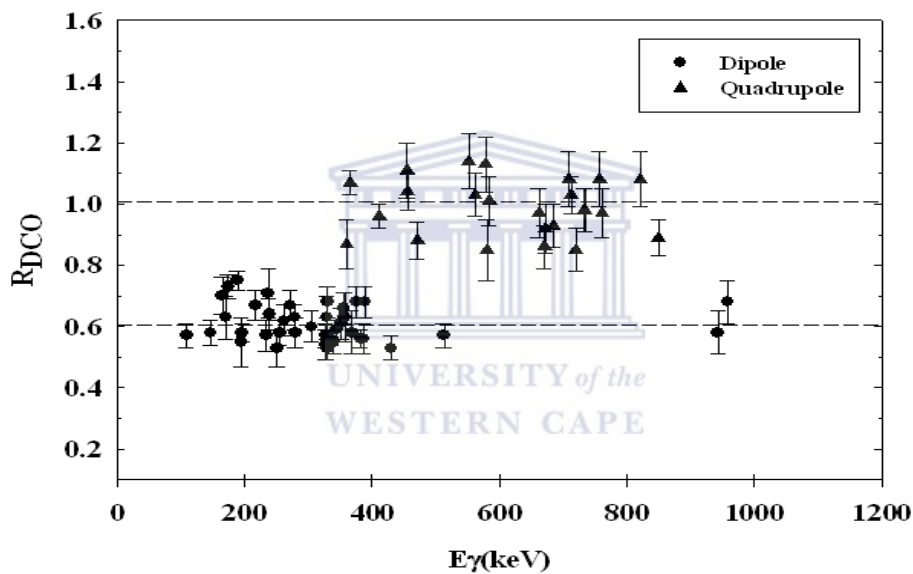


Figure 5.2: The R_{DCO} values for the γ -transitions in the ^{190}Tl decay scheme obtained by setting gates on quadrupole transitions as a function of energy.

As an example, the coincidence spectra gated on the 552 keV (E2) transition are shown in Figure 5.3 and Figure 5.4. The figures show that the γ -intensities of stretched quadrupole transitions seen by the 135° clover detectors and 90° clover detectors are almost equal, when a gate is set on the stretched quadrupole transition 552 keV. However, the γ -intensities of stretched dipole transitions seen by 135° clover detectors are roughly two-thirds of the γ -intensities of stretched dipole transitions seen by the 90° clover detectors, when the same gate is used.

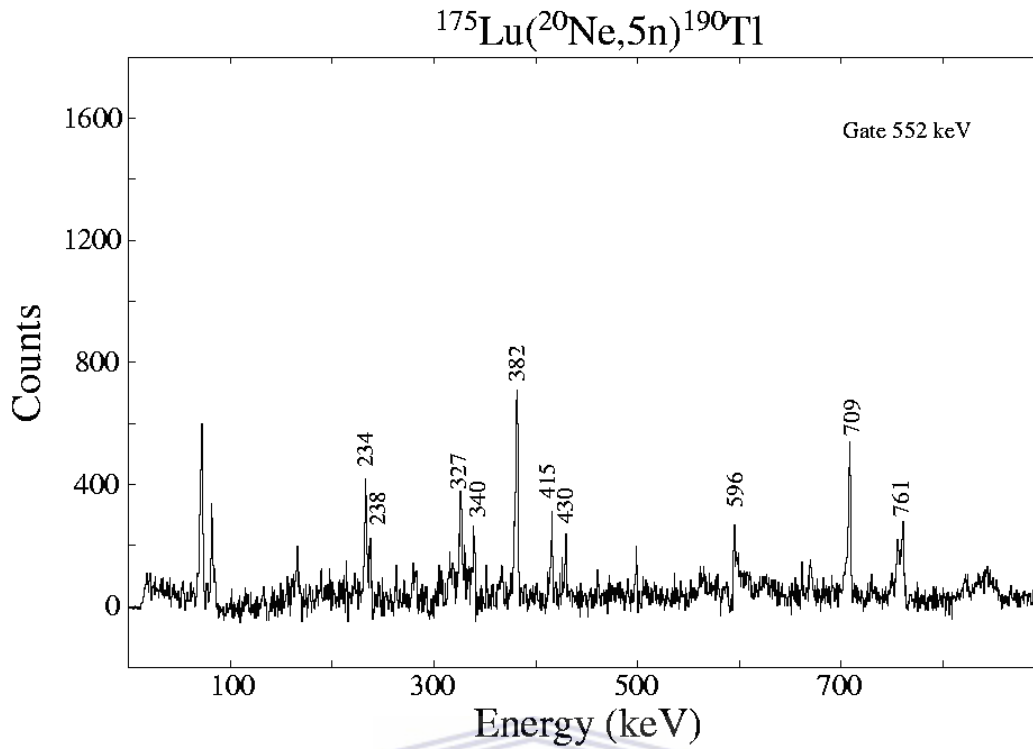


Figure 5.3: The γ - γ coincidence spectrum gated on the 552 keV transition detected in the 135° clover detectors.

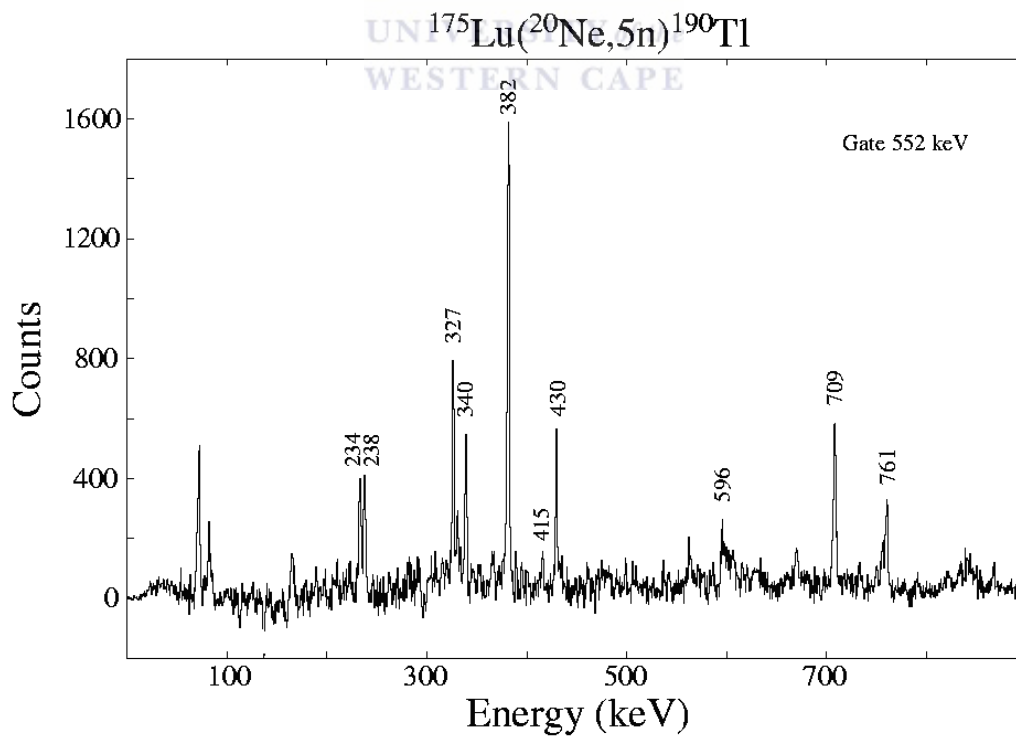


Figure 5.4: The γ - γ coincidence spectrum gated on the 552 keV transition detected in the 90° clover detectors.

The R_{DCO} values were also obtained by setting gates on previous known stretched dipole transitions. The R_{DCO} ratios measured from dipole gates strongly depend on the mixing ratio of the gated transition as well as of the transition of interest. Figure 5.5 shows the R_{DCO} values as a function of the γ -ray energy for different transitions obtained by gating on stretched dipole transitions. The Figure shows that the $\Delta I=2$ cross-over transitions tend to cluster around R_{DCO} values around 1.6. However, $\Delta I=1$ direct transitions in a band tend to cluster around R_{DCO} values of 1. The average R_{DCO} value of $\Delta I=2$ cross-over transitions was 1.62(6), while the average R_{DCO} value for $\Delta I=1$ direct transitions was 0.98(8).

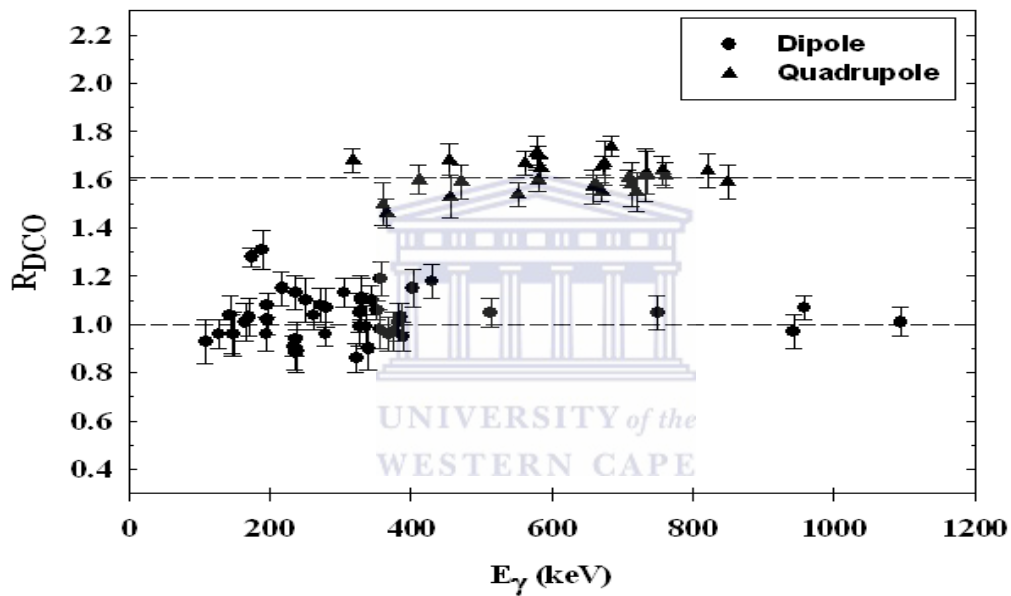


Figure 5.5: The R_{DCO} values for the γ -transitions in the ^{190}Tl decay scheme obtained by setting gates on stretched dipole transitions as a function on energy.

Examples of spectra formed by gating on a stretched dipole transition are shown in Figure 5.6 and Figure 5.7. They show that the γ -intensities of stretched dipole transitions seen by 135° clover detectors and 90° clover detectors, are almost equal when the matrix is gated on stretched dipole transition, 382 keV. However, the γ -intensities of stretched quadrupole transitions seen by the 135° set of clover detectors is roughly five-thirds of the γ -intensity of any stretched quadrupole transitions seen by the 90° clover detectors, when the matrix is gated on the 382 keV transition.

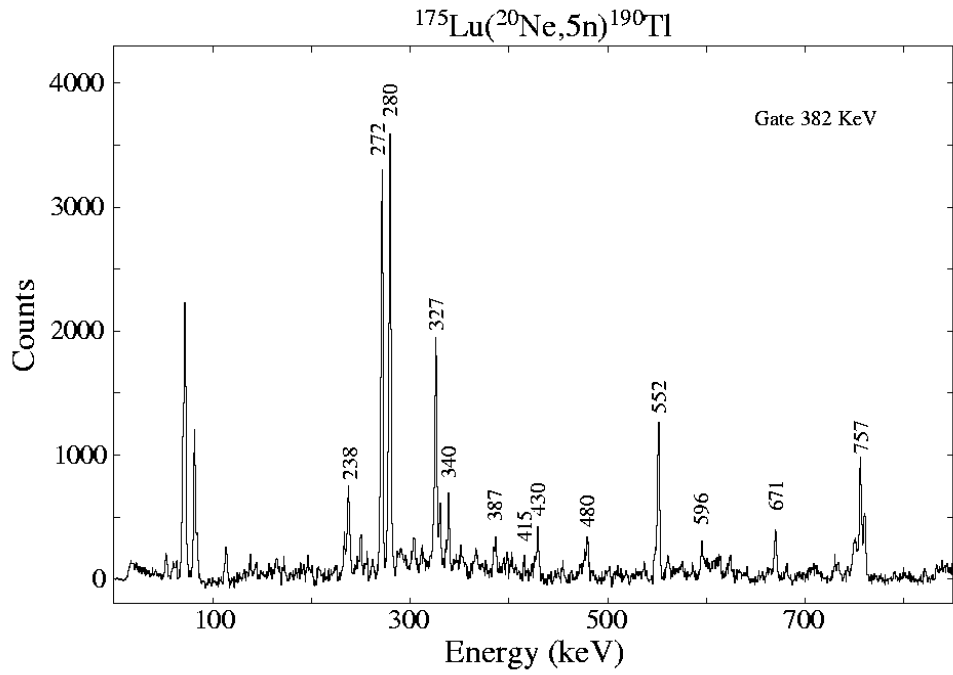


Figure 5.6: The γ - γ coincidence spectrum gated on 382 keV transitions detected in the 135° clover detectors.

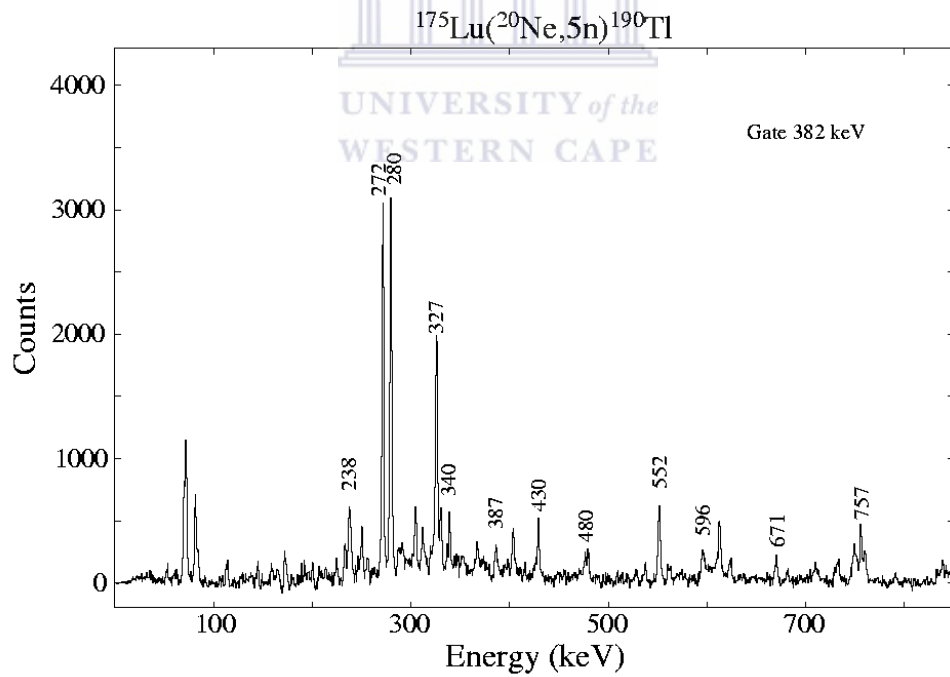


Figure 5.7: The γ - γ coincidence spectrum gated on 382 keV transitions detected in the 90° clover detectors.

5.2 Linear polarization measurements

Linear polarization measurements are used to deduce the electric and magnetic nature of γ -transitions in a decay scheme. Table 5.1 shows the expected value for the linear polarization $P(\theta)$ calculated using the angular distribution coefficients a_2 and a_4 as given in [Yam67]. If the polarization sensitivity Q of the AFRODITE clover detector resembles the polarization sensitivity Q suggested by [Jon95] as shown in Figure 3.5, then stretched E2 transitions in the 500-800 keV energy range will have a Q value between 0.18 and 0.22. As a result, the linear polarization anisotropy A_p between 0.08 and 0.11 is expected for these transitions. Stretched M1 transitions in 250-430 keV energy range will have Q values close to 0.25. Therefore, a linear polarization anisotropy A_p close to - 0.06 will be expected for stretched M1 transitions.

Figure 5.8 shows the linear polarization $P(\theta)$ values as function of the mixing ratio for mixed M1+E2 transitions. It shows that the linear polarization $P(\theta)$ values depend on the mixing ratio and single $P(\theta)$ value can correspond to more than one mixing ratio value. From Figure 5.8, the dashed line indicates the plot for $\Delta I=0$ transitions, while the solid line indicates the plot of $\Delta I=1$ transitions.

Table 5.1: Indicates the value of the linear polarization $P(\theta)$ of γ -rays for different radiation type. The γ -rays are of pure multipolarity.

Radiation type	a_2	a_4	$P(\theta)$
Stretched E1	-0.1967	0.0000	0.2687
Stretched M1	-0.1967	0.0000	-0.2687
Unstretched E1	0.3526	0.0000	-0.6420
Unstretched M1	0.3526	0.0000	0.6420
Stretched E2	0.2867	-0.0538	0.4738
Stretched M2	0.2867	-0.0538	-0.4738

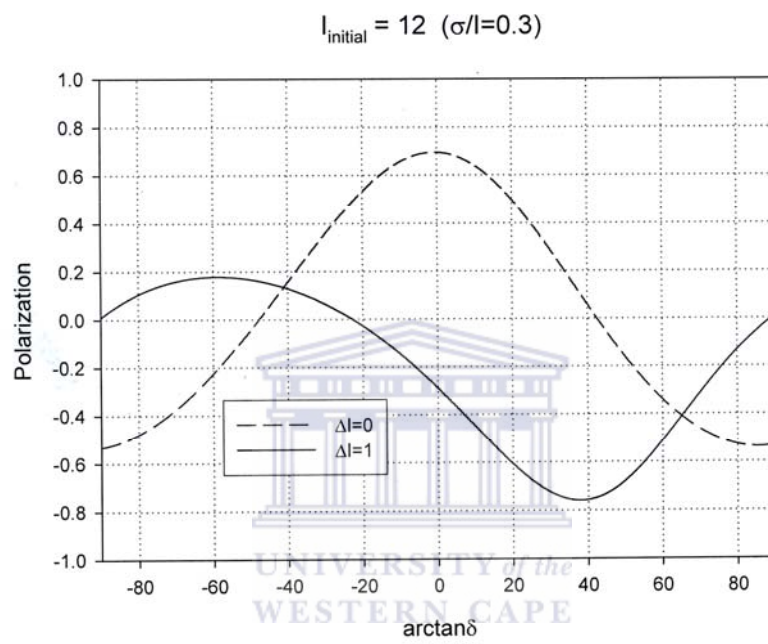


Figure 5.8: The polarization $P(\theta)$ values as a function of the mixing ratio. The dashed line indicates the plot for $\Delta I=0$ transitions. The solid line indicates the plot of $\Delta I=1$ [Bar07].

When measuring the linear polarization anisotropies A_P of transitions in the decay scheme, it does not matter whether stretched E2 and stretched M1 transitions are used as gating transitions. However, in the present data analysis, the linear polarization anisotropies were deduced using stretched E2 transitions as gating transitions. Figure 5.9 shows that the $\Delta I=2$ cross-over electric transitions in a band tend to cluster around A_P values of 0.08, while $\Delta I=1$ direct magnetic transitions in a band tend to cluster around A_P values of -0.07. The average A_P value of $\Delta I=2$ cross-over electric transitions was 0.07(4), while the average A_P value for $\Delta I=1$ direct magnetic transitions was -0.06(1).

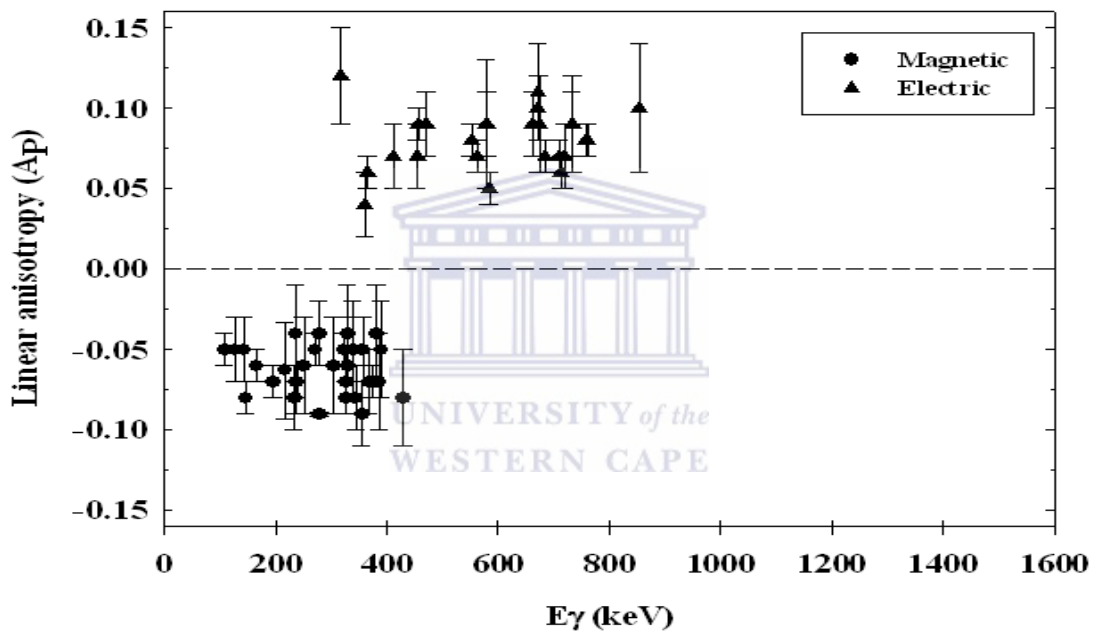


Figure 5.9: The linear polarization anisotropy as a function of energy.

The horizontal and vertical coincidence spectra were summed up to obtain the “sum spectra”. The horizontal coincidence spectrum was subtracted from the vertical coincidence spectrum to obtain the “difference” spectra. Through inspection, it was observed that in the difference coincidence spectrum the peaks for stretched M1 transitions have negative counts while the peaks for stretched E2 transitions are positive. However, due to the quality of these spectra, it was decided not to show the sum and difference spectra in this thesis.

CHAPTER 6 SPIN AND PARITY ASSIGNMENT

6.1 Band 1

The ground state of ^{190}Tl has been assigned as a 7^+ state, and the head of the band as 10^- [Ell81, Kre81]. The highest spin for Band 1 observed by [Zho05] and [Xhie05], was 18^- . Band 1 consists of two sequences of γ -cascades labeled (a) and (b) as shown in Figure 6.1. The γ -cascades (a) and (b) consist of six cross-over transitions, respectively. The newly observed cross-over transitions with energies of 472, 562, 578 and the 672 keV are seen in the sum of coincidence spectra gated on the 709 keV, 552 keV and 761 keV transitions as indicated in Figure 6.2.

The measurements of R_{DCO} and A_{P} showed that the cross-over transitions in γ -cascade (a) are stretched E2 in character (see Table 6.1). As a result, the highest level at the excitation energy of 4.095 MeV in γ -cascade (a) has a spin of 22 with negative parity.

The cross-over transitions in γ -cascade (b) are also stretched E2 in character. As a result, the highest level at the excitation energy of 3.705 MeV in γ -cascade (b) has a spin of 21 with negative parity.

The $\Delta I=1$ direct transitions in a Band 1 had a R_{DCO} value around 0.60 and 1.03 from gates set on quadrupole and dipole transitions, respectively. The linear polarization anisotropy value for these transitions was around -0.06 . These measurements are consistent with typical values of M1/E2 transitions (see Table 6.1). This support the assignment of 22^- as the highest observed state in Band 1.

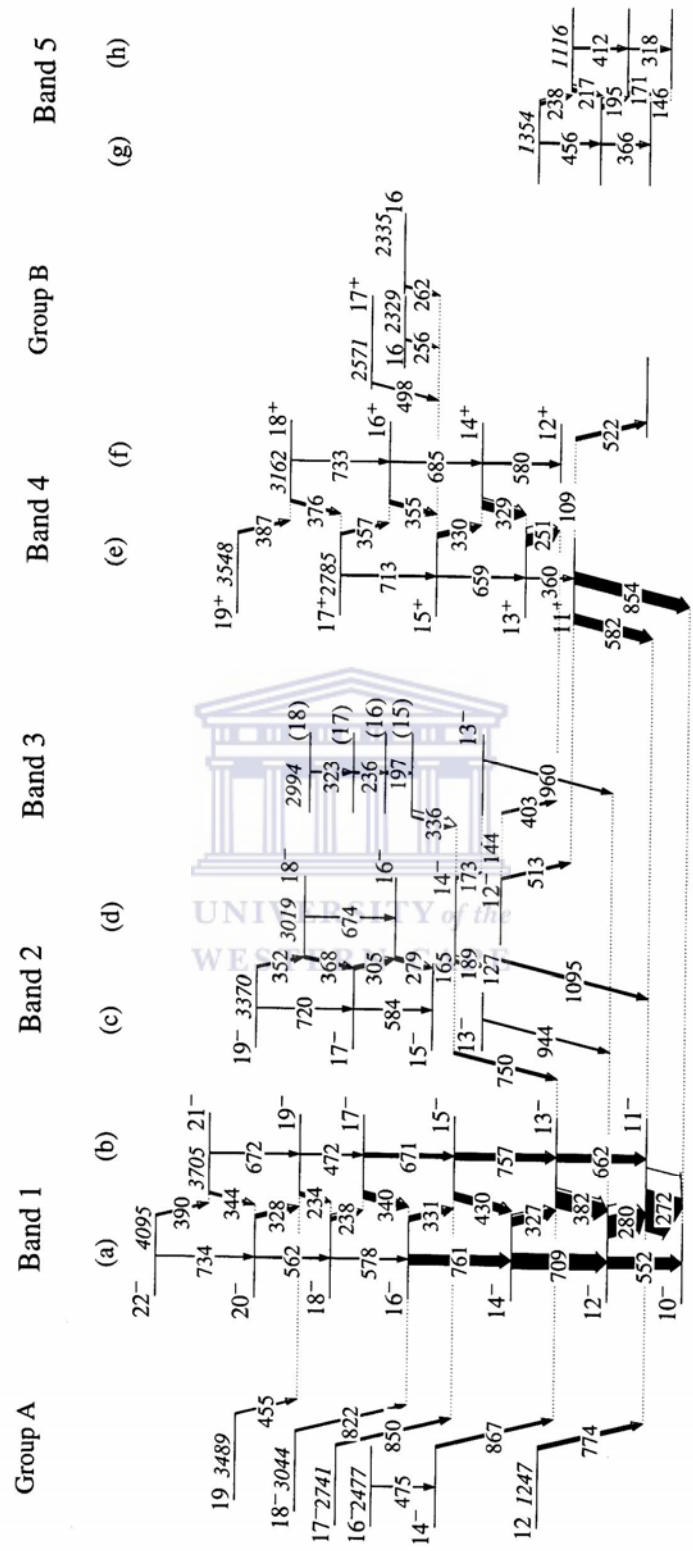


Figure 6.1: The proposed level scheme of ^{190}Tl with spin and parity assigned. The energy levels are grouped into rotational bands. The energies are given in keV.

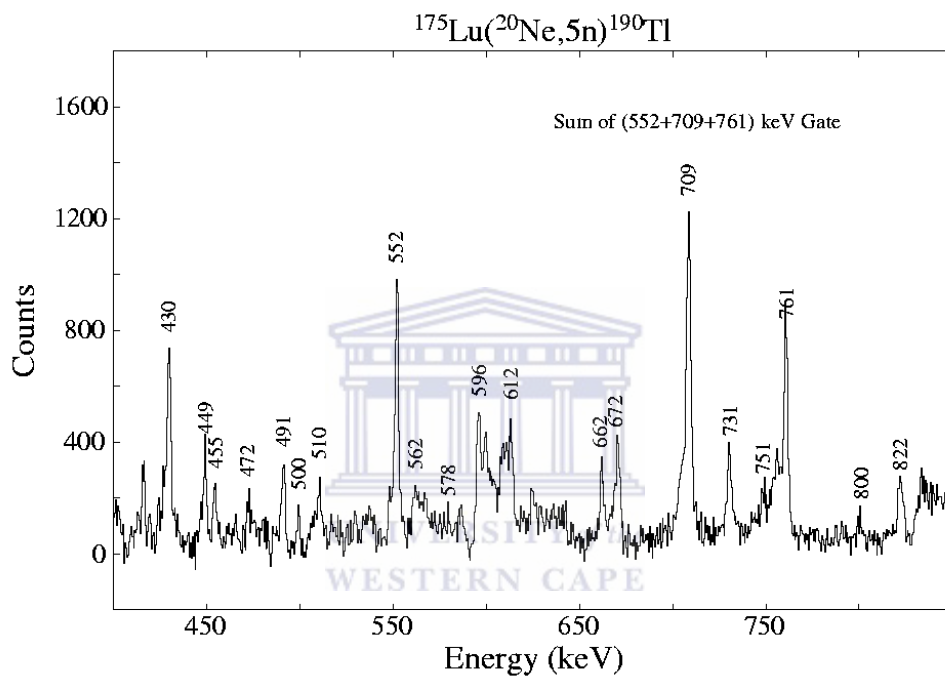


Figure 6.2: Coincidence spectrum obtained as a sum of spectra gated on the 552 keV, 709 keV, and 761 keV transitions.

Table 6.1: Gamma-ray energies, R_{DCO} ratios from coincidence spectra gated on quadrupole transitions, R_{DCO} ratios from coincidence spectra gated on dipole transitions, linear polarization anisotropy A_P , and spin and parity assignment for transitions in Band 1 of ^{190}Tl level scheme.

Band 1:

E_γ (keV) [#]	$I_i^\pi \rightarrow I_f^\pi$	$R_{DCO}(Q)$	$R_{DCO}(D)$	A_P	Multipolarity
234.3	$19^- \rightarrow 18^-$	0.57(5)	0.91(4)	-0.08(1)	M1/E2
238.5	$18^- \rightarrow 17^-$	0.64(5)	0.89(9)	-0.07(4)	M1/E2
272.1	$11^- \rightarrow 10^-$	0.67(5)	1.08(7)	-0.05(1)	M1/E2
280.2	$12^- \rightarrow 11^-$	0.58(5)	1.07(8)	-0.09(3)	M1/E2
327.0	$14^- \rightarrow 13^-$	0.54(5)	1.05(8)	-0.07(4)	M1/E2
327.8	$20^- \rightarrow 19^-$	0.57(4)	0.99(8)	-0.08(1)	M1/E2
330.6	$16^- \rightarrow 15^-$	0.68(5)	1.10(9)	-0.06(1)	M1/E2
340.0	$17^- \rightarrow 16^-$	0.55(4)	0.90(9)	-0.05(3)	M1/E2
344.4	$21^- \rightarrow 20^-$	0.59(3)	1.10(6)	-0.08(2)	M1/E2
382.2	$13^- \rightarrow 12^-$	0.56(3)	1.01(8)	-0.04(3)	M1/E2
389.7	$22^- \rightarrow 21^-$	0.68(5)	0.95(6)	-0.05(3)	M1/E2
430.2	$15^- \rightarrow 14^-$	0.53(4)	1.18(7)	-0.08(3)	M1/E2
471.7	$19^- \rightarrow 17^-$	0.88(6)	1.59(7)	0.09(2)	E2
552.4	$12^- \rightarrow 10^-$	1.14(9)	1.54(5)	0.08(1)	E2
562.1	$20^- \rightarrow 18^-$	0.88(7) [*]	1.67(5)	0.07(1)	E2
578.2	$18^- \rightarrow 16^-$	1.13(9) [*]	1.71(7)	0.09(4)	E2
662.1	$13^- \rightarrow 11^-$	0.97(8)	1.58(4)	0.09(2)	E2
671.2	$17^- \rightarrow 15^-$	0.86(7)	1.55(4)	0.10(2)	E2
672.4	$21^- \rightarrow 19^-$	0.92(8)	1.66(4)	0.11(3)	E2
709.5	$14^- \rightarrow 12^-$	1.08(9)	1.61(3)	0.07(1)	E2
734.4	$22^- \rightarrow 20^-$	0.98(7) [*]	1.63(9)	0.09(3)	E2
757.3	$15^- \rightarrow 13^-$	1.08(9)	1.64(6)	0.08(1)	E2
761.5	$16^- \rightarrow 14^-$	0.97(8)	1.62(5)	0.08(1)	E2

)^{*} γ -ray intensity measured from sum coincidence spectra gated on 709 keV, 552 keV and 761 keV transitions.

)[#] uncertainties ~ 0.3 keV, but up to 1 keV for transitions with multiple lines.

6.2 Energy levels decaying to Band 1

Several other levels were observed to decay into Band 1. These have been labeled “Group A” for convenience. It is not clear whether these levels are associated with the same intrinsic configuration. The transitions 455 keV, 774 keV, 822 keV, 850 keV and 867 keV connect levels in “Group A” to the energy levels in Band 1.

The value of R_{DCO} for the 774 keV transition from the gate set on the 272 keV transition indicated that it is of dipole in character. Therefore, a spin of 12 is tentatively assigned to the level at excitation energy of 1.247 MeV without parity.

The 867 keV transition had a R_{DCO} values of 0.63(7) and 1.03(5) from gates set of quadrupole and dipole transitions, respectively and A_{P} values of -0.05(3) as indicated in Table 6.2. This is consistent with an M1/E2 transition, and therefore a spin of 14⁻ is assigned to the level from which the 867 keV transition decays. The R_{DCO} and A_{P} values of the 475 keV transition resemble the typical values of a stretched E2 transition. As a result, the level at the excitation energy of 2.477 MeV is assigned spin and parity of 16⁻.

The 850 keV transition had a R_{DCO} ratio of 1.11(9) and 1.70(4) from gates set on quadrupole and dipole transition, respectively. The linear anisotropy A_{P} value obtained for the 850 keV transition was 0.05(2) and this is consistent with stretched E2 transition. As a result, the level at the excitation energy of 2.741 MeV is assigned spin and parity of 17⁻.

The R_{DCO} ratio for the 822 keV transition was found to be 1.08(9) and 1.64(7) from gates set on dipole and quadrupole transitions, respectively, while the A_{P} value was 0.08(4). This is consistent with typical values of stretched E2 transition, and as a result the level at the excitation energy of 3.044 MeV is assigned spin and parity of 18⁻. The measurement of R_{DCO} from gates on quadrupole transitions and A_{P} value for the 455 keV transition could not be determined. However, an R_{DCO} value of 1.11(9) was obtained when gates were set on dipole transitions. As a result, the level at excitation energy of 3.489 MeV is assigned a spin of 19 without parity.

Table 6.2: Gamma-ray energies, spin and parity assignment, R_{DCO} ratios from coincidence spectra gated on quadrupole transitions, R_{DCO} ratios from coincidence spectra gated on dipole transitions, linear polarization anisotropy A_P for transitions in “Group A” of ^{190}T level scheme.

“Group A”					
E_γ (keV) [#]	$I_i^\pi \rightarrow I_f^\pi$	R_{DCO} (Q)	R_{DCO} (D)	A_P	Multipolarity
455.5	$19^- \rightarrow 19^-$) ^a	1.11(9)) ^a) ^d
474.9	$16^- \rightarrow 14^-$	0.85(6)) ^a	0.08(2)	E2
774.4	$12^- \rightarrow 11^-$) ^e	0.73 (2)) ^a) ^d
822.0	$18^- \rightarrow 16^-$	1.08(9)	1.64(7)	0.08(4)	E2
849.9	$17^- \rightarrow 15^-$	0.89(6)	1.59(7)	0.05(2)	E2
867.3	$14^- \rightarrow 13^-$	0.63(7)	1.03(5)	-0.05(3)	M1/E2

)[#] uncertainties ~ 0.3 keV, but up to 1 keV for transitions with multiple lines.

)^a γ -transition intensity insufficient to measure.

)^d multipolarity could not be determined.

)^e the transition is not linked to any quadrupole transition.

6.3 Band 2

Transitions in Band 2 are observed for the first time. Band 2 consists of two sequences of γ -cascades, labeled (c) and (d), respectively. Band 2 is linked to Band 1 via 750 keV, 944 keV and 1095 keV transitions, and Band 4 via 403 keV and 513 keV transitions.

The first linking transition, 750 keV, had a R_{DCO} values of 0.72(6) and 1.05(7) from gates set of quadrupole and dipole transitions, respectively and A_{P} values of -0.02(1) as indicated in Table 6.3. This is consistent with an M1/E2 transition. As a result, a spin of 14^- was assigned to the level that decays to Band 1 through the 750 keV transition. The second linking transition 944 keV had a R_{DCO} values of 0.58(7) and 0.97(7) from gates set of quadrupole and dipole transition, respectively. It had a linear anisotropy value of -0.04(2) which is consistent with M1/E2 transition. As a result, a spin of 13^- was assigned to the level that decays to Band 1 through the 944 keV transition. The last linking transition (1095 keV) connecting energy levels in Band 1 and Band 2 had R_{DCO} and A_{P} values consistent with M1/E2 transition. As a result, a spin of 12^- was assigned to the level that connects the lead of Band 1 through the 1095 keV transition.

The γ -cascade (c) consists of the two cross-over transitions of energy 720 keV, and 586 keV. However, no cross-over transition covering the 165 KeV and 189 keV transitions could be observed. The measurement of R_{DCO} values showed that the 189 keV transition is stretched dipole in character. As a result, a spin of 14^- was assigned to the level above the 13^- state. The 165 keV transition had R_{DCO} and A_{P} values consisted with the typical value of M1/E2 transition. As a result, a spin of 15^- was assigned to the level linked to the 14^- state through the 165 keV transition. The two cross-over transitions in γ -cascade (c) possess stretched E2 characters. As a result, spin and parity of 19^- was deduced for the highest level at excitation energy 3.370 MeV in γ -cascade (c).

The second γ -cascade (d) contains only 674 keV cross-over transition. However, no cross-over transition covering the 127 keV and 189 keV transitions could be observed.

Also, no cross-over transition covering the 165 keV and 279 keV transitions was observed. The measurements of R_{DCO} and A_P for the 674 keV transition are consistent with typical values of stretched E2 transitions. As a result, the highest level at the excitation energy of 3.019 MeV in γ -cascade (d) has a spin of 18 with negative parity.

The measurement of R_{DCO} and A_P values for $\Delta I=1$ direct transitions in Band 2 are also consistent with typical values for M1/E2 transition (see Table 6.3). This support the assignment of 19^- as the highest observed state in Band 2.

Table 6.3: Gamma-ray energies, R_{DCO} ratios from coincidence spectra gated on quadrupole transitions, R_{DCO} ratios from coincidence spectra gated on dipole transitions, linear polarization anisotropy A_P , and spin and parity assignment for transitions in Band 2 of ^{190}Tl level scheme.

Band 2:

E_γ (keV) [#]	$I_i^\pi \rightarrow I_f^\pi$	$R_{DCO}(Q)$	$R_{DCO}(D)$	A_P	Multipolarity
127.3	$13^- \rightarrow 12^-$) ^a	0.96(6)	-0.05(2)	M1/E2
143.7	$13^- \rightarrow 12^-$) ^a	1.04(8)	-0.04(2)	M1/E2
165.3	$15^- \rightarrow 14^-$	0.70(6)	1.01(8)	-0.06(1)	M1/E2
174.4	$14^- \rightarrow 13^-$	0.78(4)	1.28(4)) ^a) ^d
189.2	$14^- \rightarrow 13^-$	0.80(3)	1.31(8)) ^a) ^d
279.1	$16^- \rightarrow 15^-$	0.63(4)	0.96(5)	-0.04(2)	M1/E2
305.4	$17^- \rightarrow 16^-$	0.60(5)	1.13(6)	-0.03(3)	M1/E2
352.3	$19^- \rightarrow 18^-$	0.61(5)	1.16(4)) ^a	M1/E2
368.3	$18^- \rightarrow 17^-$	0.58(7)	0.96(7)	-0.07(2)	M1/E2
403.2	$12^- \rightarrow 12^+$) ^a	1.15(8)	-0.03(1)	E1
513.4	$12^- \rightarrow 11^+$	0.57(4)	1.05(6)	0.04(2)	E1
584.4	$17^- \rightarrow 15^-$	1.01(8)	1.65(4)	0.05(1)	E2
674.3	$18^- \rightarrow 16^-$) ^a	1.67(9)	0.09(3)	E2
720.3	$19^- \rightarrow 17^-$	0.85(7)	1.55(8)	0.07(2)	E2
750.1	$14^- \rightarrow 13^-$	0.72(6)	1.05(7)	-0.02(1)	M1/E2
944.4	$13^- \rightarrow 12^-$	0.58(7)	0.97(7)	-0.04(2)	M1/E2
1095.0	$12^- \rightarrow 11^-$) ^a	1.01(6)	-0.03(2)	M1/E2

)[#] uncertainties ~ 0.3 keV, but up to 1 keV for transitions with multiple lines.

)^a γ -transition intensity insufficient to measure.

)^d multipolarity could not be determined.

6.4 Band 3

The energy levels in Band 3 are also observed for the first time. Band 3 is linked to the 12^- level in Band 1 via 960 keV transition. Band 3 is also linked to the energy levels in Band 2 via 336 keV transition.

The first linking transition 960 keV had an R_{DCO} value of 0.68(7) and 1.07(5) from gates set of quadrupole and dipole transition, respectively and an A_{P} value of -0.03(3). This is consistent with typical values for M1/E2 transition and therefore a spin of 13^- is assigned to the level that is connected to Band 1 through the 960 keV transition (see Table 6.4).

We could not determine the A_{P} value for the linking transition 336 keV. However, R_{DCO} value of 0.99(9) was obtained when the gates set on dipole transitions. This suggests that 336 keV has a stretched dipole character. As a result, the spin of the level linked to Band 2 through this transition is tentatively assigned as 15. The parity of this level could not be assigned due to insufficient statistics.

The transitions in Band 3 had an average R_{DCO} value of 0.96(7) from gates set on dipole transitions. In addition, negative A_{P} values were obtained for all these transitions. The measurement of R_{DCO} and A_{P} for the direct transitions in Band 3 is consistent with typical values for M1/E2 transition. Therefore, Band 3 consists of a sequence of stretched M1/E2 transitions with spin of 18 tentatively assigned to the highest level at excitation energy 2.994 MeV.

Table 6.4: Gamma-ray energies, R_{DCO} ratios from coincidence spectra gated on quadrupole transitions, R_{DCO} ratios from coincidence spectra gated on dipole transitions, linear polarization anisotropy A_P , and spin and parity assignment for transitions in Band 3 of ^{190}Tl level scheme.

Band 3:

E_γ (keV) [#]	$I_i^\pi \rightarrow I_f^\pi$	$R_{DCO}(Q)$	$R_{DCO}(D)$	A_P	Multipolarity
196.7	(16) \rightarrow (15)) ^a	1.02(6)	-0.07(1)	M1/E2
235.9	(17) \rightarrow (16)) ^a	0.88(7)	-0.08(1)	M1/E2
322.7	(18) \rightarrow (17)) ^a	0.86(6)	-0.05(3)	M1/E2
336.5	(15) \rightarrow 14 $^-$) ^a	0.99(9)) ^a) ^d
959.6	13 $^-$ \rightarrow 12 $^-$	0.68(7)	1.07(5)	-0.03(3)	M1/E2

)[#] uncertainties \sim 0.3 keV, but up to 1 keV for transitions with multiple lines.

)^a γ -transition intensity insufficient to measure.

)^d multipolarity could not be determined.

6.5 Band 4

Some of the energy levels in Band 4 were also observed in [Zho05] and [Xie05] experiment. Band 4 consists of two sequences of γ -cascades labeled (e) and (f). Band 2 is linked to the 10^- state of Band 1 via an 854 keV transition and the 11^- state of Band 1 via the 582 keV transition.

The R_{DCO} ratio for the 854 keV transition was found to be 1.04(9) from gates set on stretched M1 transitions, while the A_P value was 0.14(4) as shown in Table 6.5. This is consistent with a stretched E1 transition. In addition, the 582 keV transition had a R_{DCO} ratio of 1.70(4) from gates set on stretched M1 transition with A_P value of -0.07(1). This suggested that the 582 transition is an unstretched E1 transition. Therefore the lowest level in Band 4 is assigned as the 11^+ state. The spin assignment for this band is in agreement with that suggested by [Zho05, Xie05].

The γ -cascade (e) consists of the three cross-over transitions of energy 360 keV, 659 keV and 713 keV of stretched E2 character. As a result, spin of 17 was deduced for the level at excitation energy 2.785 MeV in γ -cascade (e). No cross-over transition covering the 376 KeV and 386 keV transitions was observed. The γ -cascade (f) consists of three cross-over transitions with energy 580 keV, 685 keV and 733 keV also of stretched E2 character. As a result, spin of 18 was deduced for the level at excitation energy 3.162 MeV in γ -cascade (f).

The average of R_{DCO} values from gates set on quadrupole and dipole transitions for $\Delta I=1$ direct transitions in Band 4 was 0.60 and 1.04, respectively. The A_P value around -0.06 was obtained, and this is consistent with M1/E2 transitions. Therefore, the highest observed state for Band 4 is the 19^+ state.

Table 6.5: Gamma-ray energies, R_{DCO} ratios from coincidence spectra gated on quadrupole transitions, R_{DCO} ratios from coincidence spectra gated on dipole transitions, linear polarization anisotropy A_p , and spin and parity assignment for transitions in Band 4 of ^{190}Tl level scheme.

Band 4:

E_γ (keV) [#]	$I_i^\pi \rightarrow I_f^\pi$	$R_{DCO}(Q)$	$R_{DCO}(D)$	A_p	Multipolarity
109.3	$12^+ \rightarrow 11^+$	0.57(4)	0.93(9)	-0.05(1)	M1/E2
251.3	$13^+ \rightarrow 12^+$	0.53(6)	1.10(9)	-0.06(3)	M1/E2
329.2	$14^+ \rightarrow 13^+$	0.63(7)	1.05(8)	-0.04(3)	M1/E2
330.3	$15^+ \rightarrow 14^+$	0.53(4)	1.11(9)	-0.04(1)	M1/E2
355.4	$16^+ \rightarrow 15^+$	0.66(5)	0.98(8)	-0.09(2)	M1/E2
357.4	$17^+ \rightarrow 16^+$	0.63(8)	1.19(7)	-0.05(2)	M1/E2
360.7	$13^+ \rightarrow 11^+$	0.87(8)	1.50(9)	0.04(2)	E2
376.1	$18^+ \rightarrow 17^+$	0.68(5)	0.97(8)	-0.07(1)	M1/E2
386.2	$19^+ \rightarrow 18^+$	0.56(5)	1.03(6)	-0.07(3)	M1/E2
521.3	$11^+ \rightarrow$) ^a	0.92(8)) ^a) ^c
580.4	$14^+ \rightarrow 12^+$	0.71(10)	1.60(5)	0.09(2)	E2
582.4	$11^+ \rightarrow 11^-$) ^a	1.70(4)	-0.07(1)	E1
659.2	$15^+ \rightarrow 13^+$) ^a	1.57(7)) ^a	E2
684.9	$16^+ \rightarrow 14^+$	0.93(7)	1.74(4)	0.07(1)	E2
712.8	$17^+ \rightarrow 15^+$	1.03(6)	1.58(9)	0.06(1)	E2
733.5	$18^+ \rightarrow 16^+$	0.98(7)	1.62(11)	0.09(2)	E2
853.9	$11^+ \rightarrow 10^-$) ^a	1.04(9)	0.10(4)	E1

)[#] uncertainties ~0.3 keV, but up to 1 keV for transitions with multiple lines.

)^a γ -transition intensity insufficient to measure.

)^c multipolarity of γ -transition cannot be deduced.

6.6 Energy levels decaying to Band 4

Three new levels were also observed and decayed to the 15^+ state of Band 4. These have been labeled “Group B” for convenience. It is not evident whether these levels are associated with the same intrinsic configuration. The transitions 256 keV, 262 keV, and 498 keV connect levels in “Group B” to the 15^+ state of Band 4.

The 498 keV transition has a R_{DCO} ratio of 0.87(10) from gates set on quadrupole transitions. The linear anisotropy A_{P} value obtained for the 498 keV transition was 0.05(1). This is consistent with stretched E2 transition, as result the level at the excitation energy of 2.571 MeV is assigned spin and parity of 17^+ .

However, the linear anisotropy A_{P} the 262 keV transition could not be determined. The R_{DCO} ratio for the 262 keV transition was found to be 0.62(5) and 1.04(6) from gates set on dipole and quadrupole transitions, respectively. This suggests that it is of stretched dipole in character, as result the level at the excitation energy of 2.335 MeV is assigned spin of 16 with no parity. The measurement of R_{DCO} from gates on dipole transition and A_{P} value for the 256 keV transition could not be determined. However, R_{DCO} value of 0.58(4) was obtained when the gates set on the quadrupole transitions. As result, the level at excitation energy of 2.329 MeV is assigned spin of 16 without parity.

Table 6.6: Gamma-ray energies, spin and parity assignment, R_{DCO} ratios from coincidence spectra gated on quadrupole transitions, R_{DCO} ratios from coincidence spectra gated on dipole transitions, linear polarization anisotropy A_P for transitions in “Group B” of ^{190}T level scheme.

“Group B”

E_γ (keV) [#]	$I_i^\pi \rightarrow I_f^\pi$	R_{DCO} (Q)	R_{DCO} (D)	A_P	Multipolarity
255.8	$16 \rightarrow 15^+$	0.58(4)) ^a) ^a) ^d
262.0	$16 \rightarrow 15^+$	0.62(5)	1.04(6)) ^a) ^d
498.4	$17^+ \rightarrow 15^+$	0.87(10)) ^a	0.05(1)	E2

)^a γ -transition intensity insufficient to measure.

)[#] uncertainties ~ 0.3 keV, but up to 1 keV for transitions with multiple lines.

)^d multipolarity could not be determined.

6.7 Band 5

The energy levels in Band 5 are entirely new. However, it was observed that Band 5 could not be linked to any other bands. Band 5 consists of two sequences of γ -cascades labeled (g) and (h). All cross-over transitions in γ -cascade (g) and (h) are stretched E2 in character while the $\Delta I=1$ direct transitions in Band 5 are M1/E2 in character. It was not possible to assign spin and parity to this band.

Table 6.7: Gamma-ray energies, R_{DCO} ratios from coincidence spectra gated on quadrupole transitions, R_{DCO} ratios from coincidence spectra gated on dipole transitions, linear polarization anisotropy A_P , and spin and parity assignment for transitions in Band 5 of ^{190}Tl level scheme.

Band 5:					
E_γ (keV) [#]	$I_i^\pi \rightarrow I_f^\pi$	$R_{DCO}(Q)$	$R_{DCO}(D)$	A_P	Multipolarity
146.4) ¹	0.58(4)	0.96(13)	-0.08(1)) ^d
171.4) ¹	0.63(7)	1.03(8)) ^a) ^d
194.5) ¹	0.55(8)	0.96(7)) ^a) ^d
217.1) ¹	0.67(5)	1.15(7)	-0.063(4)) ^d
237.6) ¹	0.71(8)	0.94(7)) ^a) ^d
318.2) ¹) ^a	1.68(5)	0.12(3)) ^d
366.0) ¹	1.07(4)	1.46(6)	0.06(1)) ^d
411.7) ¹	0.96(4)	1.60(6)	0.07(2)) ^d
456.4) ¹	1.04(6)	1.53(9)	0.09(1)) ^d

)[#] uncertainties ~ 0.3 keV, but up to 1 keV for transitions with multiple lines.

)¹ the spin and parity of energy levels cannot be determined.

)^a γ -transition intensity insufficient to measure.

)^d multipolarity could not be determined.

CHAPTER 7 SUMMARY AND CONCLUSION

The energy level scheme of ^{190}Tl has been considerably extended to higher energy levels and spins following in-beam γ -ray spectroscopy using the AFRODITE array. In the present experiment three additional pairs of rotational bands were observed as compared to the [Zho05, Xie05] experiment. One rotational band (Band5) could not be linked to any other bands in ^{190}Tl . Thus it is not certain than Band 5 is indeed in ^{190}Tl . However, the thallium x-rays peaks were observed when the symmetric matrix was gated in one of the transition in the unlinked band.

The multipolarity of the deexciting γ -transitions and relative spins and parity of levels were determined from the Directional Correlation from Oriented states (DCO) and linear polarization anisotropy measurements. The spins and parities of Band 2 and Band 4 were successfully assigned, while the levels of Band 1 were extended to 22nd state. The spins of levels in Band 3 were tentatively assigned without parity, while no spin and parity assignment was possible for Band 5.

To meaningfully describe the rotational behaviour of ^{190}Tl nucleus, the following areas of research will be carried out:

- Search for isomeric states in ^{190}Tl nucleus. An isomer is state of a nucleus above the ground state with a longer life time than excited states of the nucleus.
- The theoretical description of all the observed bands and structure in the ^{190}Tl level scheme using the total routhian surface calculations (TRS). In TRS calculations, the total routhians are calculated for different nuclear shapes of the nuclear potential and the shape of the nucleus corresponds to the minima of the TRS.

REFERENCE

- [Afr05] AFRODITE Array Operating Procedure, iThemba LABS, (2005).
- [And76] G. Andersson, S.E. Larsson, G. Leander, P. Moller, S.G. Nilsson, I. Ragnarsson, S. Aberg, R. Bengtsson, J. Dudek, B. Nerlo-Pomorska, K. Pomorski and Z. Szymanski, Nucl. Phys. **A268**, 205 (1976).
- [Bar07] R.A. Bark, Private Communication, (2007).
- [Bus02] J.T. Bushberg, J.A. Seibert, E.M. Leidholdt and J.M. Boone, by The Essential Physics of Medical Imaging. Lippincott Williams & Wilkins, pg. 38 (2002).
- [Ell81] Y.A.E. Ellis-Akovali, K.S. Toth, C.R. Bingham, H.K. Cartet and D.C. Sousa, Phys. Rev. **C23**, 480 (1981).
- [Fag59] L.W. Fagg and S.S. Hanna, Rev. Mod. Phys. **31**, 711 (1959).
- [Ham75] W.D. Hamilton, The Electromagnetic Interaction in Nuclear Spectroscopy, by North-Holland Amsterdam, pg. 582 (1975).
- [Hil53] D.L. Hill and J.A. Wheeler, Phys. Rev. **89**, 1102 (1953).
- [Hod97] P.E. Hodgson, E. Gadioli and E. Gadioli-Ebra, Introductory Nuclear Physics, by Clarendon Press Oxford, pg. 350 (1997).
- [Jon95] P.M. Jones, Nucl. Instr. and Meth. **A362**, 556 (1995).
- [Kno79] G.F. Knoll, Radiation Detection and Measurement, by John Wiley & Sons, pg. 52 (1979).
- [Kra73] K.S. Krane, R.M. Steffen and R.M. Wheeler, Nuclear Data Tables **11**, 351 (1973).
- [Kra88] K.S. Krane, Introductory Nuclear Physics, by John Wiley & Sons, pg. 199 (1988).
- [Krä89] A. Krämer-Flecken, T. Morek, R.M. Lieder, W. Gast, G. Hebbinghaus, H.M. Jager and W. Urban, Nucl. Instr. and Meth. **A275**, 333 (1989).

- [Kre81] A.J. Kreiner, C. Baktash, G. Gracia-Bermúdez, and M.A.J. Mariscotti, Phys. Rev. Lett. **47**, 1709 (1981).
- [Lan03] M.F. L'Annunzita, Handbook of Radioactivity Analysis, by Academic Press, pg. 36 (2003)
- [Lee02] J.H. Lee, C.S. Lee, J.Y. Huh, J.Y. Moon, Y.K. Kwon, Y. Gono, T. Fukuchi, S. Tanaka, T. Shinozuka, M. Fujita, A. Yamazaki, T. Sonoda, Y.K. Kim and J.S. Chai, J. of Korean Phys. Soc. **40**, 793 (2002).
- [Leo87] W.R. Leo, Technique for Nuclear and Particle Physics Experiment, by Lausanne, pg. 113 (1987).
- [Lil01] J. Lilley, Nuclear Physics Principles and Applications, John Wiley & Sons. Ltd, pg. 139 (2001).
- [Mab03] G.K. Mabala, PhD thesis, University of Cape Town, (2003).
- [Mal06] M.S. Maliage, MSc thesis, University of Western Cape, (2006).
- [Mor74] H. Morinaga and T. Yamazaki, In-Beam Gamma-Ray Spectroscopy, Elsevier North-Holland Inc. New York, pg. 14 & 54 (1974).
- [Rad95] D.C. Radford, Nucl. Instr. and Meth. **A361**, 297 (1995).
- [Ram06] T.M. Ramashidzha, MSc thesis, University of Western Cape, (2006).
- [Rin90] P. Ring and P. Schuck, The Nuclear Many-Body Problems, by Springer-Verlag Inc. pg. 6 (1980).
- [Rou01] D.G. Roux, PhD thesis, University of Cape Town, (2001).
- [Sch94] B. Schlitt, U. Mailer, H. Friedrichs, S. Albers, I. Bause, P. Von Bretano R.D. Herzberg, U. Kneissi, J. Margraf, H.H. Pitz, C. Wesselborg and A. Zilges, Nucl. Instr. and Meth. **A337**, 416 (1994).
- [Sch98] G.J. Schlitt, A.O. Macchiavelli, S.J. Astalos, R.M. Clark, R.A. Clark, M.A. Deleplangue, R.M. Diamond, P. Fallon, R. Kriecken, I.Y. Lee, R.W. Macleod, F.S. Stephens and K. Vetter, Nucl. Instr. and Meth. **A417**, 95 (1998).
- [Shi07] O.T. Shirinda, MSc thesis, University of Western Cape, (2007).

- [Sim83] J. Simpson, P.A. Butler and L.P. Ekstrom, Nucl. Instr. and Meth. **204**, 463 (1983).
- [Twi73] P.J. Twin, Nucl. Instr. and Meth. **106**, 481 (1973).
- [Xie05] C.Y. Xie, X.H. Zhou, Y.H. Zhang, Y.X. Guo, X.G. Lei, Y. Zheng, M.L. Liu, L.T. Song, H.L. Wang, W.T. Guo, H.P. Yu, L.H. Zhu, X.G. Wu and F.R. Xu, Phys. Rev. **C72**, 044302 (2005).
- [Yam67] T. Yamazaki, Nucl. Data **A3**, 1 (1967).
- [Zho05] X.H. Zhou, C.Y. Xie, Y.H. Zhang, Y.X. Guo, X.G. Lei, Y. Zheng, M.L. Liu, L.T. Song, H.L. Wang and W.T. Guo, J. Phys. (London) **G31**, S1985 (2005).

